Fall 12-2011

Optical and Magnetic Properties of FeNi Slanted Columnar Thin Films Infiltrated with PMMA and Fe_3O_4 Nanoparticles

Dan Liang
University of Nebraska–Lincoln, liangdan1984@gmail.com

Liang, Dan, "Optical and Magnetic Properties of FeNi Slanted Columnar Thin Films Infiltrated with PMMA and Fe_3O_4 Nanoparticles" (2011). *Theses, Dissertations, and Student Research from Electrical & Computer Engineering*. 28.
http://digitalcommons.unl.edu/elecengtheses/28

Optical and Magnetic Properties of FeNi Slanted Columnar Thin Films Infiltrated with PMMA and Fe_3O_4 Nanoparticles

By

Dan Liang

A THESIS

Presented to the Faculty of

The Graduate College at the University of Nebraska

In Partial Fulfillment of Requirements

For the Degree of Master of Science

Major: Electrical Engineering

Under the Supervision of Professors Eva Schubert and Mathias Schubert

Lincoln, Nebraska

December 2011

Optical and Magnetic Properties of FeNi Slanted Columnar Thin Films Infiltrated with PMMA and Fe_3O_4 Nanoparticles

Dan Liang, M.S.
University of Nebraska, 2011

Advisor: Eva Schubert and Mathias Schubert

In this thesis, dielectric polymer and magnetic nanoparticles were utilized to hybridize FeNi Slanted columnar thin films (SCTFs). Firstly Fe_3O_4 in PMMA matrix was prepared by physical blending process. Transmission electron microscopy (TEM) and scanning electron microscopy (SEM) were used to investigate the dispersion of the nanoparticles in PMMA matrix and the preparation conditions were varied to optimize the dispersion. The hybridized materials were prepared by the infiltration of PMMA and 5 wt% Fe_3O_4 nanoparticles/PMMA to the voids of FeNi SCTFs. Spin-coating and annealing process were employed to reach an excellent infiltration.

The structural property of FeNi SCTFs and FeNi SCTF composites (FeNi SCTFs after infiltration) was studied by GE and SEM. The anisotropic Bruggeman effective medium approximation (AB-EMA) was used to model the experimental data. The GE analysis successfully characterized the structural parameters of the samples and the results show the structure of nanocolumns was changed due to the infiltration. SEM result confirmed the structural property found by GE. The GE analysis also revealed a strongly anisotropic optical property of the samples. The optical constants along the three major axes of the biaxial layer can be obtained by modeling. Due to the excellent material infiltration into the void of SCTFs, the optical constants along the three major axes have enhanced greatly across the investigated spectral range.

The magnetic property of the samples was characterized by Alternating field gradient magnetometer (AGFM) and MOGE. The hysteresis loops measured by AGFM in different configurations reflected the anisotropic nature of the magnetization within the samples. The MOKE of the samples was measured in polar configuration and the corresponding complex MO tensor element was determined in the spectral range. Vector magneto-optical generalized ellipsometry (VMOGE) with the external magnetic field rotating along different loops was utilized to measure the SCTF composites. The three complex magneto-optical tensor elements were determined by the loop measurements to study the effect of the nanoparticles on the MO property of FeNi SCTFs.

Acknowledgements

I am deeply grateful to my advisers Dr. Eva Schubert and Dr. Mathias Schubert for teaching and supporting me during my study at UNL. I would like to thank them for the discussion and suggestion on my research work. With their patient and kind help, I am able to improve and finish this thesis.

I would like to thank all my colleagues in this wonderful group for not only the valuable suggestions on my research, but also the precious time we spent together. I would like to express my appreciation of Dr. Hao Wang and Dr. Daniel Schmidt's help on the experiment.

I would like to give special thanks to Dr. Tino Hofmann and Dr. Natale Ianno for being my committee members.

Last but not least, I would like to thank my parents and grandparents in China for their love, encouragement and support all the time.

Contents

List of Figures

List of Tables

Chapter 1

Introduction

Nanomaterials have been receiving enormous interests from academia, industry and government for decades, since physicist Richard Feynman firstly introduced the concept of nanomaterials by delivering a talk in 1959 entitled "There's Plenty of Room at the Bottom" (1). These materials usually have internal or surface structure with one or more dimensions in the size range from 1 nm to 100 nm(2). Within nanoscale, the materials can exhibit a great number of properties different from the ones in macroscale because of quantum size effects, quantum tunneling effects and large-scale surface. The unique and remarkable properties stemming from the extremely small feature size enable a wide range of applications in electronics, biomedicine, astronautics, etc.

Nanomaterials are mainly classified as zero-dimensional, one-dimensional, two-dimensional and three-dimensional nanostructures. Zero-dimensional nanostructure is often referred to nanoparticle with all three dimensions below 100 nm(3). These materials are highly developed and can be the basis for other nanomaterials. For example, nanoparticles can be dispersed in polymer materials to form nanocomposites that combine the desirable properties of both materials(4). The use of zero-dimensional structures has been reported on a variety of fields, for instance, drug delivery(5), quantum dots(6), and chemical catalyst(7). One-dimensional nanostructure is a nano-object with two similar external dimensions on the nanoscale and the third dimension significantly larger which includes nanofibre, nanorod, nanotube, nanowire, etc(3). Two-dimensional nanostructures possess nanoscale dimensions only in thickness and infinite length in the plane(8). Three dimensional nanostructures are emerging nanomaterials with distinct nanoscale features in arbitrary dimension. Great effort has been made on the fabrication techniques of complex three-dimensional nanostructure, because well-controlled morphology, orientation, and dimension become vital to the novel properties of this material. For instance, the self-assembly of low-dimensional building blocks is considered to be an efficient but difficult method to obtain highly-ordered three-dimensional nanostructures(9).

In terms of nanostructure fabrication, a physical vapor deposition technique called glancing angle deposition (GLAD) has been proven to be effective and convenient. In this technique, the deposition flux is incident on the substrate at an oblique angle with respect to surface normal and the substrate is rotating simultaneously(10). The shadowing effect introduced by the oblique angle can produce columnar structures while substrate rotation results in a variety of structures such as zig-zag, spirals, etc. Therefore by simply rotating the substrate in both polar and azimuthal directions one can prepare customized nanostructures such as columnar nanostructures with different shapes and helical nanostructures(10). These nanostructured materials named sculptured thin films (STFs) have been explored in various fields of applications such as sensor devices(11–13), hybrid solar cells(14,15) and engineered optical materials(16–19). Particularly magnetic nanocolumns and nanohelices have received great research attention, since the unique nanostructures can have potential use on nano storage device, magnetic actuators and perpendicular reading heads(20). Randomly distributed posts and helices can be fabricated in a one-step process from typical magnetic materials such as cobalt, nickel and iron. Periodic arrays of nanocolumns have been prepared by using substrate pre-patterning(20). The nanostructures introduce magnetic anisotropy to the thin films and lead to many interesting phenomena. For instance, the magnetic anisotropy of slanted nanocolumns is characterized by two principle axes: one parallel and the other normal to the columns(21). The magneto-optical (MO) properties of the ferrimagnetic STFs have also been investigated intensely because of their applications on thin film based MO devices such as recording devices and Faraday rotation cell(22). The researchers studied the magneto-optical Kerr effect (MOKE) of the STFs in different magnetic field orientations by measuring Kerr rotation and observing the anisotropic behaviors in Kerr effect(22–25).

A novel strategy of modifying the properties of the STFs is to alter the void fraction, composition and surface conditions through hybridization with other functional materials such as conducting polymers and nanoparticles. This hybridization process not only optimizes the host material performance but also combines each material component in an organic way, creating a new family of advanced materials for future applications. For instance, the ideal structure of a heterojunction solar cell can be consisted of a hybrid organic-metal oxide nanocolumn system with appropriate morphology control(14,26). The optical properties of the nanostructured thin films can be changed by semiconducting polymer infiltration(27) and it is indicated that the sensitivity to the dielectric constants in the void regions allows the STF composites to be used as nanosensors(21,28). The addition of nematic liquid crystals (LCs) to porous helical STFs improves the optical properties of the films and suggests a promising application in dynamically switchable device(29,30).

Due to the unique optical and magnetic properties alongside the ease of processing, hybrid nanoparticle/polymer composite is considered to be an excellent infiltration material to improve the performance of STFs. Figure 1.1 depicts the concept of infiltration of STFs with nanoparticles/polymer composites. Such slanted columnar structure with nanoparticles in figure 1.1a may have the potential application as tunable optical or magnetic devices. Periodically-arranged helical STFs shown in figure 1.1b can be fabricated from metal and infiltrated with ferrimagnetic nanoparticles to become a magnetic data storage material(31). The research work in this thesis is aimed to modify the magneto-optical (MO) response of the ferrimagnetic STFs with magnetic nanoparticle infiltration. A nanocomposite with 10 nm magnetite (Fe_3O_4) embedded in host matrix polymethylmethacrylate (PMMA) was used to fill the void of the FeNi slanted columnar thin films (SCTFs). With magnetic nanoparticles located at the interspacing of the nanocolumns, the coupling effect among the nanocolumns would enhance,

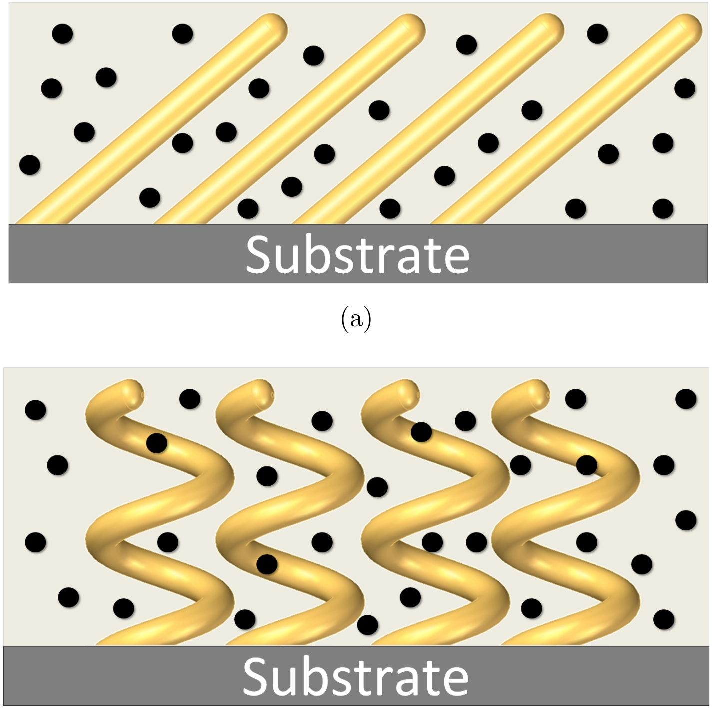

(a)

(b)

Figure 1.1: Scheme of STFs infiltrated with nanoparticle/polymer composites: (a) Slanted columnar thin film; (b) helical thin film. In the figure, the column and spiral posts in gold color denote the differently shaped nanostructure and the black spheres indicate nanoparticles.

thus the MO property of the SCTFs is expected to be influenced by the nanoparticles. Additionally, the change in the optical and structural properties of the FeNi SCTFs after polymer infiltration is of great interest for research.

In this research, a nondestructive and highly-precise methodology, spectroscopic generalized ellipsometry, is employed in order to systematically investigate the optical and MO properties of STFs/nanocomposite hybrid thin film. Due to the strong anisotropy in the structure, STFs exhibit complex optical and MO behaviors such that advanced ellipsometry techniques are required to analyze the materials. Generalized ellipsometry (GE) has proven to be an effective method to characterize complex multilayered materials with intrinsic and arbitrarily oriented anisotropy(32–38). In GE, the optical response of the materials is measured in the form of Mueller matrix elements and the anisotropic dielectric functions can be determined. GE has demonstrated great ability to study the optical dispersion and anomalous birefringence of SFTs(39–43). Magneto-optical generalized ellipsometry (MOGE) occurs if generalized ellipsometry is performed on a sample in the presence of a magnetic field. By MOGE, one can determine the magneto-optical dielectric tensors and have an insight into the magnetization dynamics of STFs under varying magnetic field(44).

The present thesis which investigates the structural, optical and magnetic properties of FeNi SCTFs infiltrated with PMMA and Fe_3O_4 nanoparticles is organized as following: In chapter 2 the growth mechanism of GLAD is introduced briefly and the deposition system used in this thesis is described. Chapter 3 reviews the recent research on preparation and magnetic property of the magnetic nanoparticles and their composites. In chapter 4, the characterization techniques such as SEM, TEM, Alternating field gradient magnetometer (AFGM) and ellipsometry are presented. The main part of this chapter is focused on the principles of spectroscopic ellipsometry. Chapter 5 depicts the experimental details on the preparation and characterization of the FeNi SCTFs infiltrated with PMMA and Fe_3O_4 nanoparticles/PMMA (FeNi SCTF composites). In chapter 6, a simple physical blending process was used to prepare Fe_3O_4 nanoparticles/PMMA composites. TEM and SEM were used to investigate the dispersion of the nanoparticles in PMMA matrix. In chapter 7, the structural and optical properties of FeNi SCTFs and FeNi SCTF composites were studied by GE and SEM. The anisotropic Bruggeman effective medium approximation (AB-EMA) was used to model the experimental data and acquire the optical constants of the samples. In chapter 8, the magnetic property of the FeNi SCTF composites is characterized with AFGM and MOGE. This chapter emphasizes on the use of an advanced ellipsometry technique vector magneto-optical generalized ellipsometry (VMOGE) to obtain the complex magneto-optical tensor. Last the experimental results and conclusion are summarized in Chapter 9.

Chapter 2

Glancing Angle Deposition

2.1 Growth Mechanism

Glancing angle deposition (GLAD) is basically a technological innovation of oblique angle deposition (OAD) by introducing substrate rotation control(21). In OAD, the trajectory of the incident vapor flux is not parallel to the substrate normal, which can generate inherently anisotropic thin films. An atomic-scale shadowing effect (also named self-shadowing), which becomes prominent with deposition angle higher than 65°, is the key to the deposition process. The self-shadowing effect involves the mechanism that the vapor can only condensate on the nuclei which nucleate on the substrate and develop to the columnar structures, while the areas behind the nuclei receive no vapor and cease growing. The left scheme in figure 2.1 describes the phenomenon of self-shadowing during the fabrication of slanted columnar. By adding substrate rotation to OAD, GLAD technique provides great opportunity to fabricate various types of nanostructures other than nanocolumns. The substrate rotation changes the direction of the incident vapor and the dynamics of self-shadowing during the deposition. Therefore the column growth can be manipulated to form desirable nanostructures by simply adjusting the manner of substrate rotation. The right scheme in Figure 2.1 depicts the formation of helical nanostructure by rotating the substrate.

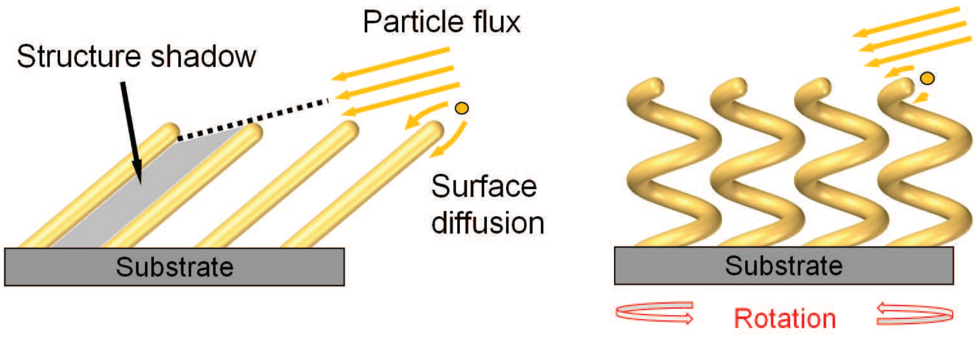

Figure 2.1: Diagram of the deposition process of typical SFTs: slanted columnar thin films (left); helical thin film (right). Scheme adapted from(44).

2.1.1 Growth of Slanted Columnar STFs

GLAD with a stationary substrate at its simplest form can be used to fabricate slanted columnar STFs. At the initial stage of the deposition, the nuclei form randomly on the substrate and become the nucleation centers for the subsequent vapor deposition. As the deposition continues, the shadowing effect dominates the process such that the nuclei receives greater amount of vapor than the shadowed areas behind them. Eventually the nuclei develop into nanocolumns which are tilted in the direction of the vapor flux approximately. In order to estimate the tilt angle of the deposited columns, much research work has been devoted to establish the relation between flux incident angle and column tilt angle(45–49). For instance, based on continuum model approach, an equation has been proposed to express the relation(48):

$$\tan\beta = \frac{2\tan\alpha}{3(1+\Phi\tan\alpha\sin\alpha)}, \tag{2.1}$$

where α is the deposition angle, β is the column tilt angle and Φ relates with the diffusion and deposition rate. Even though the equations from the literature can be consistent with the experiments in specific conditions, the columnar nanostructure have strong dependence on deposition parameters and surface properties of the materials, thus the estimation on the column tile angle can be difficult(21).

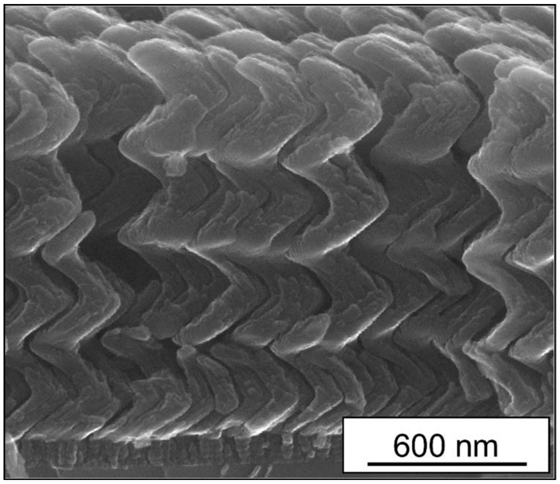

Figure 2.2: SEM cross-section image of a Si helical STF grown by GLAD(50).

2.1.2 Growth of Helical STFs

With the substrate rotation at a relatively slow rate, the nanocolumn can have sufficient time to grow along different directions, which lead to helical structure formation. The deposition parameters such as time interval of each rotation step and the deposition angle determine the fine structure of helical STFs which includes the perimeter of each loop, diameter of the columns, the number of the turns, etc. Figure 2.2 shows the cross-section SEM image of Si helical STF.

2.2 Glancing Angle Deposition System Configuration

2.2.1 Deposition System

A general experimental setup for pragmatic GLAD process is described schematically in Figure 2.3. The vapor flux is generated by electron beam evaporation of the deposition materials. The movement of the substrate is controlled by two stepper motors: one controls the angle θ between incident flux and the substrate normal; the other controls the azimuthal rotation of the substrate with respect to the substrate normal. In modern GLAD technique, computers are used to precisely manipulate the motion of the two motors through the feedback from the deposition rate monitor.

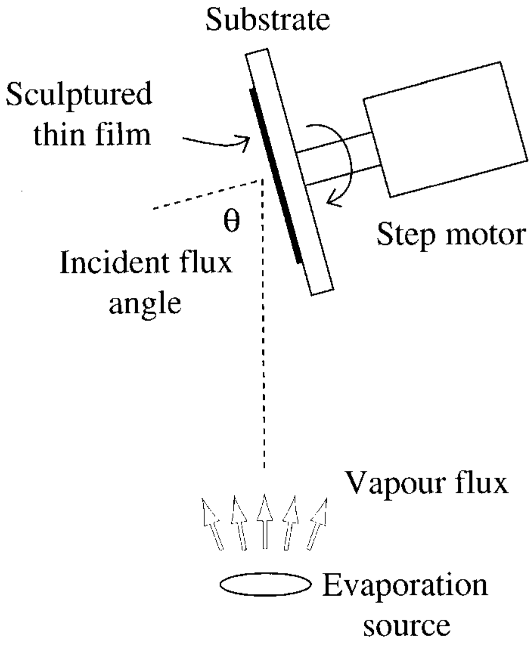

Figure 2.3: Scheme of GLAD Setup(51).

2.2.2 GLAD Apparatus

In this work, the GLAD system mainly comprises two components as shown in Figure 2.4: the deposition chamber and the load-lock chamber. The deposition chamber is an ultrahigh vacuum system (UHV) attached by a mechanical pump and a turbomolecular pump which can pump the system to a pressure of 10^{-8} mbar regularly. The electron beam evaporator system is located at the bottom of the deposition system and it is used to provide a stable vapor flux for deposition. During the evaporation, the electron gun with tungsten filament emits the electrons which can be accelerated in an electrical field and directed by a magnetic lens to hit the source material. The material loaded in a pocket is heated and then evaporated by the constant electron bombardment. The sample manipulator and deposition controller which controls the substrate rotation and monitors the deposition process respectively are also located in the deposition chamber(44).

The load-lock chamber is attached to the deposition chamber and functions as sample transfer from atmospheric pressure to high vacuum. The sample can be placed into the deposition chamber without interruption of ultra-high vacuum. A scroll vacuum pump and a turbomolecular pump attached to this chamber can produce a high vacuum as 10^{-6} mbar within 5 minutes. Once the load-lock chamber reaches the required low pressure, the gate valve connecting the two different chambers mentioned above can be opened and the sample can be translated to the sample manipulator in the deposition chamber by the sample transfer system(44).

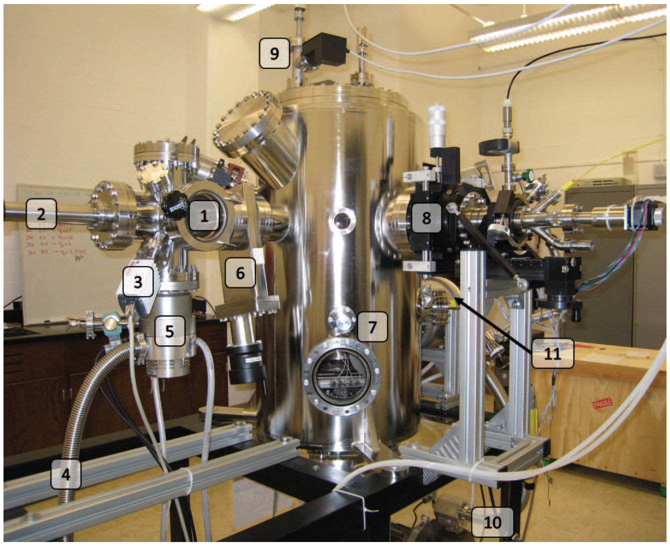

Figure 2.4: Photograph of the UHV GLAD system: (1) port for sample loading, (2) magnetically-coupled linear-rotary feedthrough with sample transfer system, (3) vacuum gauge, (4) connection to roughening pump, (5) turbo pump, (6) gate valve to deposition chamber, (7) view port with shutter and maintenance flange for electron beam evaporator system, (8) sample manipulator unit with stepper motor, (9) vacuum gauges, (10) roughening pump, and (11) turbo pump. Items (1)-(5) belong to the load-lock chamber whereas (7)-(11) are parts of the deposition chamber(44).

Chapter 3

Magnetic Nanoparticle/Polymer Composites

Magnetic nanoparticles can be considered as a zero-dimensional nanomaterial in the scale of less than 100 nm(3). This special class of material is prepared from magnetic elements such as Fe, Co, Ni, or chemical compounds such as CoFe, FePt, or oxides such as Fe_3O_4, $CoFe_2O_4$. Magnetic nanoparticles commonly exhibit unique chemical and physical properties which are different from bulk magnetic materials. For example, the magnetic nanoparticles begin to show superparamagnetism when the diameter of the nanoparticles decreases to a critical value which depends on particular material but is typically 10-20 nm(52). At such a small size, each nanoparticle becomes a single magnetic domain and shows superparamagnetic behavior such that the nanoparticles display large magnetic moment instantly in a magnetic field with negligible remanence and coercivity. Because of these features, magnetic nanoparticles are of great interest for a wide range of applications including biomedicine(53), magnetic resonance imaging(54,55), electromagnetic interference(56), data storage(57), Faraday effect(58), environmental protection(59,60) and catalysis(61,62). To seek a broader application of magnetic nanoparticles, recent research has focused on utilizing polymer as matrix material with respect to its easy processability, low cost and other functions. The combination of polymer and the nanoparticles aims to preserve properties of both components or to increase the functions by combining the properties of both components, which leads to more opportunities of nanoparticle applications.

3.1 Preparation of Nanoparticle/Polymer Composites

The fabrication technology for nanoparticles/polymer composites is a significant issue since the excellent performance of the composites is determined by a successful combination of two constituents into a single material. The importance of this technology is considered for all sorts of nanoparticle/polymer composites, thus the knowledge of this technology can be applied to magnetic nanoparticle/polymer composites as well. Numerous effects have been taken to search an effective and simple method to obtain highly-quality composites.

The most common preparation technique involves blending or mixing of the two components directly using polymer in solutions or melt form. Sonication or mechanical blending process is normally used in this method. This simple physical process causes a weak interaction between nanoparticles and polymer by hydrogen bonding or van der Waals forces only. The insufficiency of this technique lies in the possible agglomeration of nanoparticles in the polymer matrix due to the incomplete contact between the two different components. Additionally, the solution blending method fails in the case of insoluble polymer.

Another effective method to synthesize nanoparticles/polymer composites is to introduce an intimate combination at a molecular level by chemical route. In this synthesis, a strong chemical covalent bond between the two phases is formed by in-situ polymerization of the monomers. After polymerization, the polymer entraps or encapsulates the nanoparticles rather than simple blending or mixing(63). The process is described in Figure 3.1.

Surfactant and polymer coatings are also employed to prepare composites with good dispersion of nanoparticles in the polymer matrix. In the absence of repulsive forces, the nanoparticles tend to agglomerate in the host matrix because of the van der Waals attraction(64) and magnetic attraction in the case of magnetic

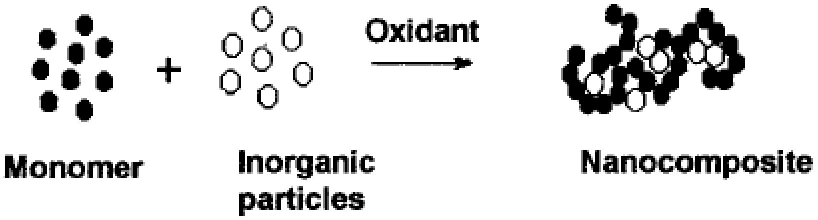

Figure 3.1: The in-situ chemical route for synthesis of nanoparticles/polymer composites(63).

particles. To solve this problem, one can attach the surfactant or polymer physically or chemically to the nanoparticle surface to create repulsion to balance the attractive force(52). Using surfactants or coupling agents has been the common route to disperse nanoparticles in polymer(65,66). More recently, polymer coating method has received much interest. The polymer coating mostly formed by in-situ polymerization can increase the compatibility of the nanoparticles with the organic phase and also protect the nanoparticles from oxidation(67). For magnetic nanoparticles, the suitable coating polymers include poly(pyrrole), poly(aniline), poly(alkylcyanoacrylates), poly(methylidene malonate), and polyesters, and their copolymers(68–71). Magnetite nanoparticles which are used in the present thesis favor the polymers containing functional groups such as carboxylic acids, phosphates, and sulfates(52). Biocompatible polymer-coated magnetic nanoparticles have been applied to the biomedical fields such as magnetic-field-directed drug targeting and magnetic resonance imaging(72,73).

3.2 Magnetic Properties of Magnetic Nanoparticles and Their Composites

The interesting properties of magnetic nanoparticles and their composites have been studied intensively by many researchers. For example, the research has been conducted to estimate the single domain size for different nanoparticle materials. The equation to calculate the critical diameter of the nanoparticles in the size of single domain is deduced by using the balance condition that the magnetostatic energy is equal to the domain wall energy:

$$D_c \approx 18\frac{\sqrt{AK_{\text{eff}}}}{\mu_0 M^2}, \tag{3.1}$$

where A is the exchange constant, K_{eff} is the anisotropy constant, μ_0 is the vacuum permeability and M is the saturation magnetization(74). The typical diameters calculated by this equation are 15 nm for hcp Co, 7 nm for fcc Co, 15 nm for Fe, 55 nm for Ni, and 128 nm for Fe_3O_4(74). However, the critical diameter is also strongly affected by particle shape and the estimation above does not consider nanoparticle interaction. The relaxation time of the magnetic moment for nanoparticles is determined by the Néel-Brown expression:

$$\tau = \tau_0 \exp\left(\frac{K_{\text{eff}}V}{k_B T}\right), \tag{3.2}$$

where k_B is the Boltzmann constant, V is the particle volume, T is the temperature and τ_0 is approximately 10^{-9} s(75). The nanoparticles can only show superparamagnetic state when the particle magnetic moment is reversed at a time scale shorter than the experimental measurement time, otherwise the nanoparticles are in the blocked state. The blocking temperature T_B which separates the two states depends on K_{eff}, V, the applied field and the experimental measurement time(52). Fe nanoparticles (20 nm in diameter)/PMMA composites were synthesized with different nanoparticle concentrations and the hysteresis loop measurements at different temperatures show the composites exhibit a mixture of single-domain and multi-domain behavior(76). C. Baker *et al.* prepared Fe oxide/Fe core shell nanaoparticles with different sizes and dispersed the nanoparticles in PMMA matrix. The experiment indicates that the interaction of the nanoparticles decreases as the particles were separated from each other. This interaction decrease results in larger coercivity and slower relaxation rate(77). Uniform dispersion of 10 nm Fe_3O_4 coated with oleic acid was achieved by simple sonication and subsequent spin-coating process. The blocking temperature can be observed in the zero-field-cooling (ZFC) data and the superparamagnetic property of the nanoparticles was retained in the polymer matrix(56). A. Ceylan *et al.* reported a formation of chain-like Fe nanoparticle cluster in polymer matrix. The magnetic response of composites displayed a nonmonotonic tendency as the nanoparticle concentration increased, which can be explained by the varying amount of the chain-like nanoparticle clusters(78).

The magneto-optical (MO) properties of the magnetic nanoparticles and their composites have also attracted significant attention from research. For instance, the MO response of Fe_3O_4 core/PMMA shell nanoparticles were dispersed in PMMA. From the Faraday rotation measurement, it was found that the Faraday rotation of the composites have an obvious dependence on nanoparticle concentration, the wavelength of the measurement, and the shape of the nanoparticles. Furthermore, the Faraday rotation angle data as a function of applied magnetic field can be fitted by a modified Langevin function:

$$m(H,T) = \sum_i N_i m_i [\coth(\frac{\mu_0 m_i H}{k_B T}) - \frac{k_B T}{\mu_0 m_i H}], \tag{3.3}$$

where N_i denotes the number of noninteracting particles per unit volume, m_i is the moment of each nanoparticle, H is the applied field, T is the temperature, k_B is the Boltzmann constant, and the sum accounts for all particles with different moments(58). Kalska *et al.* have deposited Co nanoparticle films on Al and Si substrates and measured the MO Kerr effect spectra. The 10 nm Co nanoparticles showed superparamagnetism while the 12 nm ones exhibited ferromagnetism which was a deviation from the Langevin function. It was also found that all the nanoparticle systems showed an opponent MO behavior compared with the bulk Co material(79). The optical and MO properties of Fe nanoparticles with diameters ranging from 5 to 8 nm embedded in amorphous Al_2O_3 were investigated with spectroscopic ellipsometry. Effective medium approximations were used to analyze the experimental data. Good agreement between model and experimental data were found for the nanoparticles with a diameter above 4 nm. Both optical and MO parameters varied as a function of the nanoparticle diameter(80). In a different report, gold and magnetite nanoparticles have been bonded with an organic molecular. The MO Faraday rotation and ellipticity of dual nanoparticle clusters can be changed greatly due to the electromagnetic interaction between those two nanoparticles(81). MO Kerr effect studies have been conducted on the magnetic nanoparticles $M_{0.5}Fe_{2.5}O_4$ (M=Fe, Co, Mn, and Ni) and the change of MO Kerr spectra due to different substitutes on Fe position was investigated(82). A highly transparent Lithium Ferrite nanoparticle/ethyl(hydroxyethyl)cellulose (EHEC) was prepared by in-situ hydrolysis. The faraday rotation of the film increased with decreasing wavelength and it was indicated that this magnetic hybrid film has applications on novel field-responsive devices(83). D. Smith *et al.* reported that the peak position of the Faraday rotation spectrum of Fe_3O_4 nanoparticles/PMMA composites was dependent on nanoparticle concentration and geometric concentration. A red shift and broadening of the main spectral feature were observed for the 8 nm nanoparticle system(84). A. Dzarrova *et al.* synthesized Fe_3O_4 nanoparticles via a biomineralization process and showed magneto-induced linear and circular anisotropy caused by chain effect of the nanoparticles. Using the classic Langevin model the authors determined an average number of 12 nanoparticles per chain which was consistent with the TEM result(85).

Chapter 4

Characterization Methods

4.1 Electron Microscopy

Transmission electron microscopy (TEM) has become one powerful method to investigate various features of materials including crystal structure, dimension, composition, defects and so on. In this technique the electron beam is employed as the imaging source. Due to the short wavelength of the electron wave, the theoretical resolution limit of TEM can be 0.3 $\AA$. The resolution of TEM method can be about 3 $\AA$ for many modern instruments and better than 2 $\AA$ for special high-voltage instruments. During the operation, the electrons are emitted by the electron gun and accelerated by high voltage(typically 100-300 kV). The electrons enter the optical system and are focused on the imaging device. The optical system is composed of mainly condenser lens, objective lens and projection lens. The electrons firstly form a beam after passing the condenser lens and strike on the sample. Secondly the objective lens focus the electron beam which penetrates the sample. The projector lenses are used to guide the electron beam to the imaging device. By adjusting the objective aperture in the back focal plane, one can select the Bragg diffraction from the sample such that the diffraction pattern of the sample can be recorded in the imaging system to reflect the crystal feature of the materials. Electron diffraction and high-resolution imaging exist as the two main functions of TEM.

Scanning electron microscope (SEM) is an another microscopy technology using an electron beam to scan the sample surface to obtain various information on materials such as surface morphology, chemical composition, *et al.* In this characterization method, high-energy electrons generated thermally by filament cathode interact with the sample to produce many sorts of signals from the materials including secondary electrons, back-scattered electrons, Auger electrons and so on. For example, the imaging function of SEM utilizes the secondary electrons to reflect the topological information on material surface. Normally the sample for SEM is required to be electrically conductive or conductive at least on the surface. Non-conductive samples need to be coated with a conductive ultrathin film by sputtering technique. The common coating materials include gold, chromium, carbon and so on. However, it is possible that the extra coating can change the morphology of the material surface.

4.2 Alternating Field Gradient Magnetometer

Alternating field gradient magnetometer (AFGM) is an instrument which measures the magnetization via magnetic flux change induced by sample vibration. In this technique, a magnetic sample is attached at the end of an nonmagnetic rod and placed into a fixed dc magnetic field(86). An alternating field gradient is produced by an electromagnet and a pair of gradient coils respectively as shown in Figure 4.1. During the measurement, the gradient coil pair can apply an alternating force to the sample which causes the sample vibration. The rod also oscillates with the sample vibration. The piezoelectric crystal connected to the rod can generate a voltage signal proportional to the vibration amplitude(86). Since the vibration amplitude is proportional to the magnetic moment of the sample, the sample magnetization can be obtained from the voltage signal(86). The limiting sensitivity of the commercial AFGM is approximately 10^{-6} emu(86).

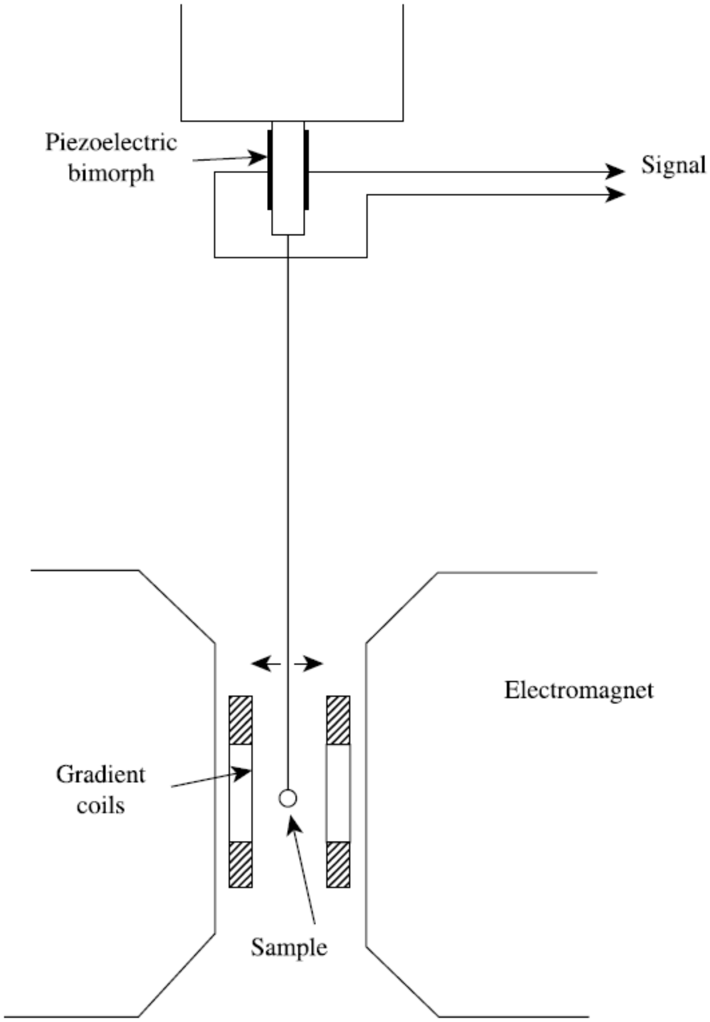

Figure 4.1: Scheme of AFGM from (86).

4.3 Spectroscopic Ellipsometry

4.3.1 General Description

Ellipsometry is a characterization method which can be used to analyze the change in the polarization state of the light after reflection or transmission on a sample. Ellipsometry can be employed to investigate material properties, such as optical constants, thin film thickness, material composition and so on. The ellipsometry measurement process is shown schematically in Figure 4.2. Upon reflection of parallel and perpendicular polarized lights (p- and s-polarized lights) on the sample, the polarization state shows changes in both amplitude and phase. For p-polarized light, the electric field is parallel to the plane of incident while s-polarized light is perpendicular. The two parameters Ψ and Δ measured by ellipsometry denote the amplitude ratio and phase difference between p- and s-polarized lights respectively, as shown in the following equation:

$$\rho \equiv \tan\Psi \exp(\mathrm{i}\Delta) \equiv \frac{r_p}{r_s} \equiv \left(\frac{E_{rp}}{E_{ip}}\right) \Bigg/ \left(\frac{E_{rs}}{E_{is}}\right), \tag{4.1}$$

where r_p and r_s are the Fresnel coefficients for p- and s-polarized lights respectively(87). Thus

$$\tan\Psi = |r_p|/|r_s|,\ \ \Delta = \delta_{rp} - \delta_{rs}. \tag{4.2}$$

When light propagates in a medium with the complex refractive index N as

$$N \equiv n + \mathrm{i}k, \tag{4.3}$$

the electromagnetic wave in the medium can be described as follows:

$$\begin{aligned} E &= E_0 \exp\left[\mathrm{i}\left(\frac{2\pi N}{\lambda}x - \omega t + \delta\right)\right] \\ &= E_0 \exp\left(-\frac{2\pi k}{\lambda}x\right) \exp\left[\mathrm{i}\left(\frac{2\pi n}{\lambda}x - \omega t + \delta\right)\right]. \end{aligned} \tag{4.4}$$

where n is refractive index, k is the extinction coefficient, E_0 is the amplitude of the electric field, ω is the angular frequency of the wave, λ is the wavelength of the wave in vacuum, and δ is the initial phase(87). As known from the Equation 4.4, the

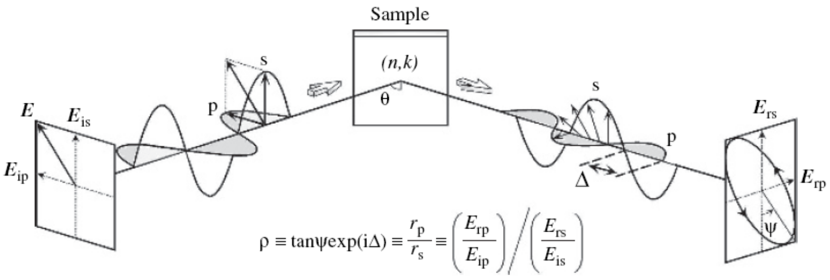

Figure 4.2: The scheme of ellipsometry measurement(87).

wavelength of the electromagnetic wave in the medium is λ/n. If the proportional constant is neglected, the light intensity can be expressed by

$$I = |E|^2 = \left| E_0 \exp\left(-\frac{2\pi k}{\lambda}x\right)\right|^2 = |E_0|^2 \exp\left(-\frac{4\pi k}{\lambda}x\right), \tag{4.5}$$

which indicates the light intensity decreases with $\exp\left(-2\pi kx/\lambda\right)$ when the light travels along the x direction in the absorbing medium(87). Therefore, as the light propagates through the medium the polarization state of the light is influenced by the n and k values. As we know from Equation 4.1, the ellipsometry measures the change of the polarization state between incident and reflected light, and by applying Fresnel equations the n and k values of the medium can be determined by analyzing the two ellipsometry parameters Ψ and Δ. When ellipsometry is performed in a wide range of the light wavelength, spectroscopic ellipsometry is used for the terminology.

4.3.2 Jones Matrix and Mueller Matrix

The polarization state of light can be presented by the Jones Vector which is defined by the electric field vector along x and y directions. For example, the polarization state of the light traveling in z direction with two electric field components oscillating in x and y directions can be expressed by the Jones vector as follows(87):

$$\mathbf{E}(z,t) = \exp\left[\mathrm{i}(kz - \omega t)\right] \begin{bmatrix} E_{x0}\exp\left(\mathrm{i}\delta_x\right) \\ E_{y0}\exp\left(\mathrm{i}\delta_y\right) \end{bmatrix}. \tag{4.6}$$

In general, by omitting the term $\exp\left[\mathrm{i}(kz-\omega t)\right]$ this equation can be simplified to(87)

$$\mathbf{E}(z,t)=\begin{bmatrix}E_{x0}\exp\left(\mathrm{i}\delta_x\right)\\E_{y0}\exp\left(\mathrm{i}\delta_y\right)\end{bmatrix}. \tag{4.7}$$

In ellipsometry measurement, the Jones matrix shown in Equation 4.8 can be used to represent the sample properties which are responsible for the change of the polarization state after the light reflection. In the equation, the Jones matrix $\mathbf{J}$ connects the incident polarized light (A_p, A_s) and the reflected light (B_p, B_s). The Jones matrix contains four complex-valued elements. For isotropic materials, the Jones matrix only contains the diagonal elements r_{pp} and r_{ss} which are the Fresnel reflection coefficients. On the other hand, both the diagonal and the off-diagonal elements of the Jones matrix are nonzero for anisotropic materials. r_{ps} represents the conversion of s-polarization into p-polarization while r_{sp} represents the conversion of p-polarization into s-polarization after reflection.

$$\begin{pmatrix}B_p\\B_s\end{pmatrix}=J\begin{pmatrix}A_p\\A_s\end{pmatrix}=\begin{pmatrix}r_{pp}&r_{ps}\\r_{sp}&r_{ss}\end{pmatrix}\begin{pmatrix}A_p\\A_s\end{pmatrix}. \tag{4.8}$$

Mueller matrix is another method to describe the propagation of polarized or partially polarized light through an optical system. In this method, the incident and emergent Stokes vectors are transformed by a Mueller matrix. The 4×4 matrix corresponds to the optical response of a material. The four Stokes parameters grouped in the column vector $\mathbf{S}$ are defined as

$$\begin{pmatrix}S_0\\S_1\\S_2\\S_3\end{pmatrix}=\begin{pmatrix}I_p+I_s\\I_p-I_s\\I_{45}-I_{-45}\\I_R-I_L\end{pmatrix}, \tag{4.9}$$

where I_p, I_s, I_{45}, I_{-45}, I_R and I_L denote the intensities for the p-, s-, $+45°$, $-45°$, right-handed and left-handed circularly polarized light components respectively(32). As shown in Equation 4.10, the Mueller matrix transforms the input Stokes vector to the output vector.

$$\begin{pmatrix}S_0\\S_1\\S_2\\S_3\end{pmatrix}_{\text{output}}=\begin{pmatrix}M_{11}&M_{12}&M_{13}&M_{14}\\M_{21}&M_{22}&M_{23}&M_{24}\\M_{31}&M_{31}&M_{33}&M_{34}\\M_{41}&M_{42}&M_{43}&M_{44}\end{pmatrix}\begin{pmatrix}S_0\\S_1\\S_2\\S_3\end{pmatrix}_{\text{input}}. \tag{4.10}$$

The Mueller matrix elements can be calculated by the following functions of Jones matrix elements(88):

$$M_{11} = \frac{1}{2}(r_{pp}r^*_{pp} + r_{ss}r^*_{ss} + r_{sp}r^*_{sp} + r_{ps}r^*_{ps}), \tag{4.11a}$$

$$M_{12} = \frac{1}{2}(r_{pp}r^*_{pp} - r_{ss}r^*_{ss} - r_{sp}r^*_{sp} + r_{ps}r^*_{ps}), \tag{4.11b}$$

$$M_{13} = Re(r_{pp}r^*_{sp} + r^*_{ss}r_{ps}), \tag{4.11c}$$

$$M_{14} = Im(r_{pp}r^*_{sp} + r^*_{ss}r_{ps}), \tag{4.11d}$$

$$M_{21} = \frac{1}{2}(r_{pp}r^*_{pp} - r_{ss}r^*_{ss} + r_{sp}r^*_{sp} - r_{ps}r^*_{ps}), \tag{4.11e}$$

$$M_{22} = \frac{1}{2}(r_{pp}r^*_{pp} + r_{ss}r^*_{ss} - r_{sp}r^*_{sp} - r_{ps}r^*_{ps}), \tag{4.11f}$$

$$M_{23} = Re(r_{pp}r^*_{sp} - r^*_{ss}r_{ps}), \tag{4.11g}$$

$$M_{24} = Im(r_{pp}r^*_{sp} - r^*_{ss}r_{ps}), \tag{4.11h}$$

$$M_{31} = Re(r_{pp}r^*_{ps} + r^*_{ss}r_{sp}), \tag{4.11i}$$

$$M_{32} = Re(r_{pp}r^*_{ps} - r^*_{ss}r_{sp}), \tag{4.11j}$$

$$M_{33} = Re(r_{pp}r^*_{ss} + r^*_{ps}r_{sp}), \tag{4.11k}$$

$$M_{34} = Im(r_{pp}r^*_{ss} - r^*_{ps}r_{sp}), \tag{4.11l}$$

$$M_{41} = -Im(r_{pp}r^*_{ps} + r^*_{ss}r_{sp}), \tag{4.11m}$$

$$M_{42} = -Im(r_{pp}r^*_{ps} - r^*_{ss}r_{sp}), \tag{4.11n}$$

$$M_{43} = -Im(r_{pp}r^*_{ss} + r^*_{ps}r_{sp}), \tag{4.11o}$$

$$M_{44} = Re(r_{pp}r^*_{ss} - r^*_{ps}r_{sp}), \tag{4.11p}$$

where $*$ denotes the conjugate value of the Jones matrix element.

4.3.3 Dielectric Tensor in Anisotropic Materials

In non-cubic solids, the dielectric constants can be expressed by a complex-valued second-rank symmetric tensor ε in Cartesian coordinates (x, y, z):

$$\mathbf{D} = \varepsilon_0(\mathbf{E}+\mathbf{P}) = \varepsilon_0\varepsilon\mathbf{E} = \varepsilon_0 \begin{pmatrix} \varepsilon_{xx} & \varepsilon_{xy} & \varepsilon_{xz} \\ \varepsilon_{xy} & \varepsilon_{yy} & \varepsilon_{yz} \\ \varepsilon_{xz} & \varepsilon_{yz} & \varepsilon_{zz} \end{pmatrix} \mathbf{E}, \tag{4.12}$$

where the displacement $\mathbf{D}$, polarization field $\mathbf{P}$, and electric field $\mathbf{E}$ are given along the unit directions $\mathbf{x}$, $\mathbf{y}$, $\mathbf{z}$ (ε_0 is the vacuum permittivity)(89). The tensor ε generally varies as a function of the photon energy $\hbar\omega$ of the incident light, which is referred to the dielectric function or dielectric dispersion.

The intrinsic polarization $\mathbf{P}$ is responsible for the dielectric response of the materials and can be described by linear superposition of polarizations along the unit cell axes $\mathbf{a}$, $\mathbf{b}$ and $\mathbf{c}$:

$$\mathbf{P} = \varrho_a(\mathbf{aE})\mathbf{a} + \varrho_b(\mathbf{bE})\mathbf{b} + \varrho_c(\mathbf{cE})\mathbf{c}, \tag{4.13}$$

where ϱ_a, ϱ_b and ϱ_c are the complex-valued scalar major polarizabilities along each cell axis. The three major polarizabilities obey Kramers-Kronig consistency and have dispersion according to the photon energy $\hbar\omega$. The unit cell axes $\mathbf{a}$, $\mathbf{b}$ and $\mathbf{c}$ are also referred to the major polarizability axes.

An orthogonal rotation matrix $\mathbf{A}$ can be used to connect the Cartesian laboratory coordinate (x, y, z) with the Cartesian auxiliary coordinate system (ξ, η, ζ), which is defined as follows:

$$\mathbf{A} = \begin{pmatrix} \cos\psi\cos\varphi - \cos\theta\sin\varphi\sin\psi & -\sin\psi\cos\varphi - \cos\theta\sin\varphi\sin\psi & \sin\theta\sin\varphi \\ \cos\psi\cos\varphi + \cos\theta\sin\varphi\sin\psi & -\sin\psi\cos\varphi + \cos\theta\sin\varphi\sin\psi & -\sin\theta\cos\varphi \\ \sin\theta\sin\psi & \sin\theta\cos\psi & \cos\theta \end{pmatrix}, \tag{4.14}$$

where φ, θ and ψ are the three Euler angles for the rotation(89). The rotation procedure is depicted in the Figure 4.3. In applying the rotation matrix, firstly the coordinate is rotated by φ around the z-axis; subsequently the system is rotated by θ around the new x-axis; finally the system is rotated by ψ around the ζ-axis to become the Cartesian auxiliary coordinate system (ξ, η, ζ).

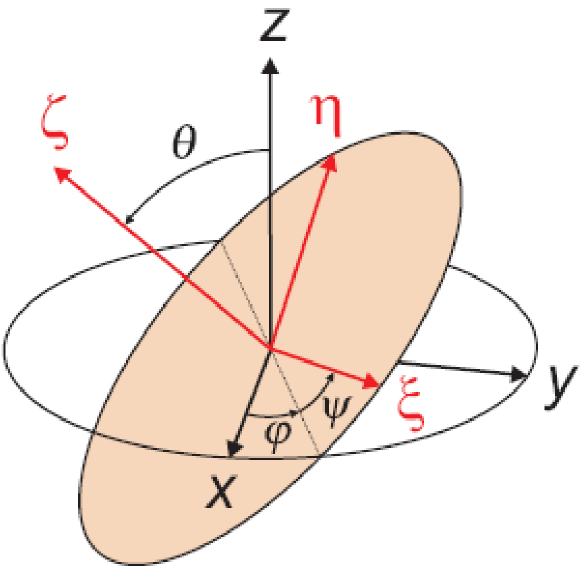

Figure 4.3: Definition of the Euler angles φ, θ and ψ and the orthogonal rotations as provided by rotation matrix $\mathbf{A}$. $(x,\ y,\ z)$ and $(\xi,\ \eta,\ \zeta)$ are referred as the Cartesian laboratory coordinate and the Cartesian auxiliary coordinate system respectively(44).

For a material with orthorhombic, tetragonal, hexagonal, trigonal and cubic symmetry, a rotation matrix $\mathbf{A}$ independent of wavelength can be found such that ε has a diagonal form in the coordinate system $(\xi,\ \eta,\ \zeta)$:

$$\varepsilon = \mathbf{A} \begin{pmatrix} \varepsilon_a & 0 & 0 \\ 0 & \varepsilon_b & 0 \\ 0 & 0 & \varepsilon_c \end{pmatrix} \mathbf{A}^{-1}, \tag{4.15}$$

where ε_a, ε_b, and ε_c are the dielectric constants in the major polarizability axis system $(a,\ b,\ c)$(44) and $\varepsilon_j = 1 + \varrho_j$ $(j = a, b, c)$. This diagonal tensor in the equation above can be employed to express the optical constants of materials. For example, in an isotropic system it is found that ε_a=ε_b=ε_c. In this case, the dielectric constant is a scalar and $\mathbf{D}$=$\varepsilon_0\varepsilon\mathbf{E}$. For uniaxial materials with tetragonal, hexagonal and trigonal symmetry, the dielectric constants can be described as ε_c along c-axis and ε_a=$\varepsilon_b\neq$ ε_c along the other two axes. The biaxial materials

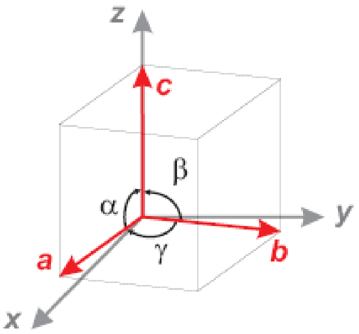

Figure 4.4: Definition of α, β and γ. The scheme depicts a crystallographic unit cell with the major axes $\mathbf{a}$, $\mathbf{b}$ and $\mathbf{c}$. α, β and γ are the angles between $\mathbf{a}$, $\mathbf{b}$ and $\mathbf{c}$. For example, with monoclinic symmetry, $\varepsilon_a \neq \varepsilon_b \neq \varepsilon_c$ and $\beta \neq \alpha = \gamma = 90°$; with triclinic symmetry, $\varepsilon_a \neq \varepsilon_b \neq \varepsilon_c$ and $\alpha \neq \beta \neq \gamma \neq 90°$ (44).

(triclinic, monoclinic and orthorhombic materials) have dielectric constants as $\varepsilon_a \neq \varepsilon_b \neq \varepsilon_c$.

For biaxial materials in non-Cartesian systems such as monoclinic and triclinic materials, an additional projection matrix $\mathbf{U}$ is required to compose a virtual orthogonal basis (90):

$$\mathbf{U} = \begin{pmatrix} \sin\alpha & (\cos\gamma - \cos\alpha\cos\beta)(\sin\alpha)^{-1} & 0 \\ 0 & (1-\cos^2\alpha - \cos^2\beta - \cos^2\gamma + 2\cos\alpha\cos\beta\cos\gamma)^{\frac{1}{2}}(\sin\alpha)^{-1} & 0 \\ \cos\alpha & \cos\beta & 1 \end{pmatrix}, \tag{4.16}$$

where α, β and γ are the internal angles between the major polarizability axes $\mathbf{a}$, $\mathbf{b}$ and $\mathbf{c}$. As shown in Figure 4.4, c-axis is chosen to be coincide with the z-axis while a-axis is located within the x-z plane. For instance, the dielectric tensor of monoclinic system is as follows:

$$\varepsilon_m = \mathbf{U} \begin{pmatrix} \varepsilon_a & 0 & 0 \\ 0 & \varepsilon_b & 0 \\ 0 & 0 & \varepsilon_c \end{pmatrix} \mathbf{U}^T = \begin{pmatrix} 1+\varrho_a & 0 & 0 \\ 0 & 1+\sin^2\beta\varrho_b & \sin\beta\cos\beta\varrho_b \\ 0 & \sin\beta\cos\beta\varrho_b & 1+\cos^2\beta\varrho_b+\varrho_c \end{pmatrix}, \tag{4.17}$$

where ϱ_a, ϱ_b and ϱ_c are the polarizability along each axis $\mathbf{a}$, $\mathbf{b}$ and $\mathbf{c}$ (44).

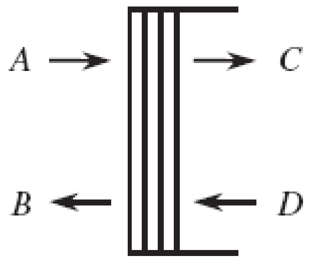

Figure 4.5: Schematic presentation of incident (A), reflected (B), and transmitted (C) plane waves across a sample with plane parallel interfaces, and multiple layer stacks at the front side of the supporting substrate. D modes (if present) are incident from the right. The substrate may totally absorb C and/or D(89).

4.3.4 Light Propagation in Stratified Anisotropic Materials

The 4×4 matrix formulism provides a general approach to describes the light propagation in stratified anisotropic materials. In this formulism, a global transfer matrix $\mathbf{T}$ is used to describe the optical response of the stratified materials to the incident light (Shown in Figure 4.5):

$$\begin{pmatrix} A_s \\ B_s \\ A_p \\ B_p \end{pmatrix} = \mathbf{T} \begin{pmatrix} C_s \\ D_s \\ C_p \\ D_p \end{pmatrix} . \tag{4.18}$$

where A_s, A_p and B_s, B_p denote the complex amplitudes of the incident and reflected lights (p- and s-polarized lights) respectively.

If the light propagates in the stratified materials, the transfer matrix $\mathbf{T}$ can be written as a product of all n partial transfer matrices $\mathbf{T}_p$:

$$T = L_a^{-1} T_{p1}^{-1} \ldots T_{pn}^{-1} L_f, \tag{4.19}$$

where L_a and L_f are the matrices for the incident and exit media respectively(33), each $\mathbf{T}_p$ describes the optical response of one homogenous layer.

Furthermore the partial transfer matrix $\mathbf{T}_p$ can be obtained from the first order Maxwell equations which Berreman derived in 1972 as follows(33):

$$\partial_z \Psi(z) = \mathrm{i} k_0 \Delta(z) \Psi(z), \tag{4.20}$$

where

$$\Psi(z) = (E_x, E_y, H_x, H_y)^T(z),\ k_0 = \frac{\omega}{c}. \tag{4.21}$$

In Equation 4.21, the E and H represent the electric and magnetic fields respectively, ω is the angular frequency and c is the light velocity in vacuum. Also it should be noted that $(E_x, E_y, H_x, H_y)^T$ denotes the transposed vector and Δ is the wave transfer matrix of the layer(33). Δ is a 4×4 matrix expressed as:

$$\Delta = \begin{pmatrix} -k_x\frac{\varepsilon_{31}}{\varepsilon_{33}} & -k_x\frac{\varepsilon_{32}}{\varepsilon_{33}} & 0 & 1-\frac{k_x^2}{\varepsilon_{33}} \\ 0 & 0 & -1 & 0 \\ \varepsilon_{23}\frac{\varepsilon_{31}}{\varepsilon_{33}} - \varepsilon_{21} & k_x^2 - \varepsilon_{22} + \varepsilon_{23}\frac{\varepsilon_{32}}{\varepsilon_{33}} & 0 & k_x\frac{\varepsilon_{23}}{\varepsilon_{33}} \\ \varepsilon_{11} - \varepsilon_{13}\frac{\varepsilon_{31}}{\varepsilon_{33}} & \varepsilon_{12} - \varepsilon_{13}\frac{\varepsilon_{32}}{\varepsilon_{33}} & 0 & -k_x\frac{\varepsilon_{13}}{\varepsilon_{33}} \end{pmatrix}, \tag{4.22}$$

where $k_x \equiv n_a \sin\Phi_a$, n_a is the complex refractive index of incident isotropic medium and Φ_a is the angle of incidence(33). If the single layer is homogeneous and the characteristic matrix Δ is independent on z, the solution of Equation 4.21 can be simplified to

$$\Psi(z+d) = \exp\left(\mathrm{i}\frac{\omega}{c}\Delta d\right)\Psi(z) = \mathbf{T}_p\Psi(z), \tag{4.23}$$

thus

$$\mathbf{T}_p \equiv \exp\left(\mathrm{i}\frac{\omega}{c}\Delta d\right). \tag{4.24}$$

By applying the theorem of Cayley-Hamilton, the partial transfer matrix $\mathbf{T}_p$ can be calculated by a finite series of expansion up to the power of n-1:

$$\mathbf{T}_p \equiv \exp\left(\mathrm{i}\frac{\omega}{c}\Delta d\right) = \beta_0\mathbf{I} + \beta_1\Delta + \beta_2\Delta^2 + \beta_3\Delta^3, \tag{4.25}$$

where n is the rank of the matrix(33). The scalars β_i must obey the following linear equations:

$$\exp\left(\mathrm{i}\frac{\omega}{c}q_k d\right) = \sum_{j=0}^{3} \beta_j q_k^j,\ \ k = 1, \ldots, 4. \tag{4.26}$$

where q_k are the eigenvalues of the matrix Δ(33). Each solution corresponds to one of the four plane waves in the homogeneous medium. The two solutions with positive real parts represent the forward-traveling plane waves and the other two with negative real parts are due to the backward-traveling plane waves.

Based on the equations above, a 4×4 matrix formalism can be established and then utilized to calculated the Jones matrix elements. The transfer matrix **T** can be expressed as follows(33):

$$\begin{pmatrix} A_s \\ B_s \\ A_p \\ B_p \end{pmatrix} = \mathbf{T} \begin{pmatrix} C_s \\ D_s \\ C_p \\ D_p \end{pmatrix} = \begin{pmatrix} T_{11} & T_{12} & T_{13} & T_{14} \\ T_{21} & T_{22} & T_{23} & T_{24} \\ T_{31} & T_{31} & T_{33} & T_{34} \\ T_{41} & T_{42} & T_{43} & T_{44} \end{pmatrix} = \begin{pmatrix} C_s \\ 0 \\ C_p \\ 0 \end{pmatrix} \tag{4.27}$$

The exiting medium is assumed to be half infinite at the back side, thus only two amplitudes for the transmitted p and s modes C_p and C_s exist. The Jones matrix elements can be expressed with the transfer matrix **T** elements by following equations(87):

$$r_{pp} = \left(\frac{B_p}{A_p}\right)_{A_s=0} = \frac{T_{11}T_{43} - T_{13}T_{41}}{T_{11}T_{33} - T_{13}T_{31}}, \tag{4.28a}$$

$$r_{sp} = \left(\frac{B_s}{A_p}\right)_{A_s=0} = \frac{T_{11}T_{23} - T_{13}T_{21}}{T_{11}T_{33} - T_{13}T_{31}}, \tag{4.28b}$$

$$r_{ss} = \left(\frac{B_s}{A_s}\right)_{A_p=0} = \frac{T_{21}T_{33} - T_{23}T_{31}}{T_{11}T_{33} - T_{13}T_{31}}, \tag{4.28c}$$

$$r_{ps} = \left(\frac{B_p}{A_s}\right)_{A_p=0} = \frac{T_{33}T_{41} - T_{31}T_{43}}{T_{11}T_{33} - T_{13}T_{31}}. \tag{4.28d}$$

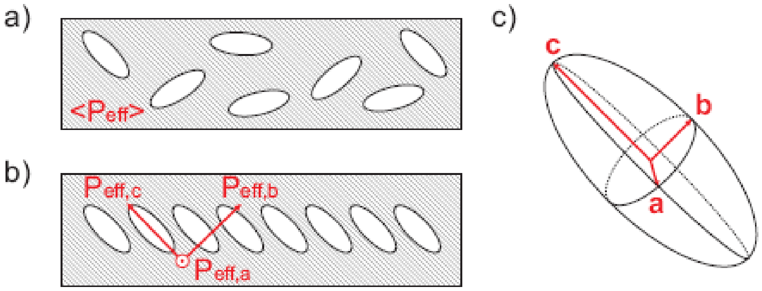

Figure 4.6: Scheme of AB-EMA: (a) the inclusions randomly distributed in the host medium with an isotropic effective polarizability ; (b) the inclusions orderly distributed in the host medium with three effective polarizabilities; (c) the individual elliptical inclusions(44).

4.3.5 Anisotropic Bruggeman Effective Medium Approximation

Effective medium approximation (EMA) theories have been established to model the optical constants of the composites comprised of two or more other materials. Bruggeman proposed the EMA expressed by following equation(32):

$$\sum_{i=1}^{n} f_i \frac{\varepsilon_i - \varepsilon}{\varepsilon_i + 2\varepsilon} = 0. \tag{4.29}$$

where ε is the dielectric function of the host, f_i is the volume fraction of the i^{th} component, ε_i is the dielectric function of the i^{th} component. The Bruggeman EMA has been successfully applied to model the surface roughness.

More recently the anisotropic Bruggeman EMA (AB-EMA) has been developed to model the optical response of the materials consisting of ordered inclusions and homogeneous host medium. As shown in Figure 4.6, with the elliptical inclusions randomly distributed in the host, the composite exhibits an isotropic effective polarizability, while the polarizability becomes biaxial with the inclusions orderly distributed in the host medium. The dielectric functions in the three major polarizability axes for two-phase composites are expressed as following(44):

$$f\frac{\varepsilon_i - \varepsilon_{\mathrm{eff,j}}}{\varepsilon_{\mathrm{eff,j}} + L_j^D(\varepsilon_i - \varepsilon_{\mathrm{eff,j}})} + (1-f)\frac{\varepsilon_m - \varepsilon_{\mathrm{eff,j}}}{\varepsilon_{\mathrm{eff,j}} + L_j^D(\varepsilon_m - \varepsilon_{\mathrm{eff,j}})} = 0, \quad j = a, b, c, \tag{4.30}$$

where ε_i and f are the dielectric function and volume fraction of the inclusions respectively, ε_m and (1-f) are the dielectric function and volume fraction of the host medium. L_a^D, L_b^D, L_c^D are the three depolarization factors along the three major polarizability axes **a**, **b** and **c**, which accounts for the anisotropic optical property in the composites. The sum of the three depolarization factors must follow(91,92):

$$L_a^D + L_b^D + L_c^D = 1, \tag{4.31}$$

with

$$0 \le L_j^D \le 1, \quad j = a, b, c. \tag{4.32}$$

The depolarization factors correspond to charge screening effects which are related with shapes of the inclusions. For instance, $L_a^D = L_b^D = L_c^D = 1/3$ for spherical inclusions(44).

4.3.6 Generalized Ellipsometry

Generalized ellipsometry (GE) adapts the 4×4 formalism to analyze the complex anisotropic stratified materials. GE parameters for reflection are define with normalized Jones matrix elements as follows(32):

$$\frac{r_{pp}}{r_{ss}} \equiv R_{pp} = \tan\Psi_{pp}\exp(\mathrm{i}\Delta_{pp}), \tag{4.33a}$$

$$\frac{r_{ps}}{r_{pp}} \equiv R_{ps} = \tan\Psi_{ps}\exp(\mathrm{i}\Delta_{ps}), \tag{4.33b}$$

$$\frac{r_{sp}}{r_{ss}} \equiv R_{pp} = \tan\Psi_{sp}\exp(\mathrm{i}\Delta_{sp}). \tag{4.33c}$$

where Ψ_{pp}, Δ_{pp}, Ψ_{ps}, Δ_{ps}, Ψ_{sp} and Δ_{sp} are the six real-valued parameters presented by Jones matrix elements. The six parameters are only sufficient for the non-depolarized light conditions. When the sample or optical ellipsometer components cause the light depolarization, the Mueller matrix elements are employed to present the GE data(37). For an anisotropic medium, the off-diagonal elements of both matrices are nonzero. Also the GE measurement are conducted at multiple sample azimuth orientations and angles of incident.

4.3.7 Magneto-Optical Generalized Ellipsometry

Magneto-optical generalized ellipsometry (MOGE) is capable of analyzing the non-symmetric dielectric constants due to the magneto-optical properties of the anisotropic materials with arbitrary magnetization direction. The dielectric function of the magneto-optical materials is composed of a symmetric (**s**) and an anti-symmetric (**a**) tensor(32) accounting for the dielectric and magneto-optical response respectively:

$$\varepsilon_{ij} = s_{ij} + a_{ij}, s_{ij} = s_{ji}, a_{ij} = a_{ji}, \tag{4.34}$$

where s_{ij} and a_{ij} are the elements of a 3×3 tensor matrix. Through the same method shown in section 4.3.4, the characteristic coefficient matrix Δ of the magneto-optical layer and the eigenvalues of Δ can be obtained. Therefore the transfer matrix $\mathbf{T}_p$ for the magneto-optical layer can be calculated from Equation 4.25 and 4.26.

The general form of the dielectric tensor of a magneto-optical medium in the presence of an external magnetic field can be described as the sum of the symmetric dielectric and non-symmetric magneto-optical tensors(93):

$$\varepsilon = \varepsilon^D + \varepsilon^{MO} = \begin{pmatrix} \varepsilon_{xx} & \varepsilon_{xy} & \varepsilon_{xz} \\ \varepsilon_{xy} & \varepsilon_{yy} & \varepsilon_{yz} \\ \varepsilon_{xz} & \varepsilon_{yz} & \varepsilon_{zz} \end{pmatrix} + \begin{pmatrix} 0 & \mathrm{i}\varepsilon^P_{xy} & -\mathrm{i}\varepsilon^T_{xz} \\ -\mathrm{i}\varepsilon^P_{xy} & 0 & \mathrm{i}\varepsilon^L_{yz} \\ \mathrm{i}\varepsilon^T_{xz} & -\mathrm{i}\varepsilon^L_{yz} & 0 \end{pmatrix}, \tag{4.35}$$

where ε^P_{xy}, ε^T_{xz} and ε^L_{yz} are off-diagonal elements of the magneto-optical tensor ε^{MO}. The three elements ε^P_{xy}, ε^T_{xz} and ε^L_{yz} are assumed to be a linear function of the sample magnetization and correspond to the magnetization along the Cartesian laboratory axis **z**, **y** and **x** respectively.

The magneto-optical effect describes the change of the polarization state upon the reflection of light from a magnetic material in the presence of an external field. MOGE can be used to study the magneto-optical Kerr effect (MOKE). In a MOKE measurement, commonly three different configurations can be employed: polar, longitudinal and transverse configuration. In a polar measurement, the external magnetic field is perpendicular to the sample surface as the light beam is incident on the sample surface. In a longitudinal measurement the magnetic field is parallel to the plane of incidence while in a transverse measurement, the field is perpendicular to the plane of incidence. MOKE measurement in the present thesis was performed with an octupole vector magnet installed on an ellipsometer stage such that the measurement can be done with the external magnetic field in arbitrary directions. The ellipsometer can monitor the magneto-optical response of the sample at each field orientation. The details of the measurement setup is described in next chapter.

Chapter 5

Experiment

5.1 Material Preparation

5.1.1 Fabrication of FeNi Alloy Slanted Columnar Thin Films

Nickel-iron (FeNi) alloys are a class of soft magnetic materials which generally contain 50-80 wt% of Ni(86). FeNi is notable for its high permeability in low fields and its ultra low coercivity. Additionally the films of FeNi can be fabricated easily by using common evaporation techniques. For the fabrication of FeNi slanted columnar thin films (SCTFs), the GLAD system described in section 2.2 was used. The deposition source materials composed of 81 wt% of Ni, 15 wt% of Fe and 5 wt% of Mo were purchased from the Kurt J. Lesker Company in form of pellets. During the deposition, the FeNi pellets were placed in graphite liners. (001) Si substrates with a approximately 2 nm native silicon oxide top layer have been used. The power of the electron-beam during the bombardment of the source material was controlled by the emission current to keep the deposition rate constantly between 4 to 5 $\mathring{A}$/s. The deposition rate was monitored by a quartz crystal microbalance. The deposition was conducted for 680 s at a deposition angle of 85° with no substrate rotation. The pressure in the chamber was maintained at 5.3×10^{-9} mbar in the deposition.

5.1.2 Preparation of Fe_3O_4 Nanoparticles/PMMA Composites

Polymethylmethacrylate (PMMA) with the weight average molecular mass $M_w = 120,000$ and the glass transition temperature $T_g = 99\ ^\circ C$ was purchased from Sigma-Aldrich. The Fe_3O_4 nanoparticles purchased from Sigma-Aldrich were dispersed in toluene with a nanoparticle concentration of 5 mg/mL. The average diameter of the nanoparticles is about 10 nm. The Fe_3O_4 nanoparticles were coated with oleic acid to prevent agglomeration and improve the solubility toluene. The magnetization of the nanoparticles is 45 emu/g (at ambient temperature under 4500 Oe) and the density of the dispersion is 0.865 g/mL at 25 °C. During the preparation, first PMMA was added to toluene and subsequently the solution was sonicated for 2.5 h in order to reach a complete dissolution of the polymer in toluene. Secondly, Fe_3O_4 nanoparticles in different weight percentages were added to the prepared PMMA/toluene solution. For example, 5 wt% Fe_3O_4 nanoparticles/PMMA denotes that the weight ratio of Fe_3O_4 nanoparticles and PMMA is 5:95. The mixture was treated with sonication to facilitate an uniform dispersion of the nanoparticles in solutions.

5.1.3 Preparation of FeNi SCTFs infiltrated with PMMA and 5 wt% Fe_3O_4 nanoparticles/PMMA

First, FeNi slanted columnar thin films (SCTFs), 5 wt% Fe_3O_4 nanoparticles/PMMA composites (5 wt% Fe_3O_4 nanoparticles/PMMA) and pristine PMMA in toluene were prepared respectively with the method described in the former two sections. Before use, the FeNi SCTF was cleaved carefully into two pieces. Subsequently, Fe_3O_4 nanoparticles/PMMA was spin-coated onto one piece of FeNi SCTF at 3000 rpm for 60 s while pristine PMMA in toluene was spin-coated onto the other piece at the same spin-coating condition. The former sample is referred to FeNi SCTFs infiltrated with 5 wt% Fe_3O_4 nanoparticles/PMMA and the latter to FeNi SCTFs infiltrated with PMMA. The two samples are termed FeNi SCTF composites in this thesis for convenience. Finally both samples were dried in the oven at 100 °C to remove the toluene. Another purpose of drying at the temperature well above T_g of PMMA is that, the molten state of the polymer can ameliorate the infiltration into the void of the SCTFs(94).

5.2 Characterization

5.2.1 Transmission Electron Microscopy

Transmission electron microscopy (TEM) was employed to investigate the dispersion of the Fe_3O_4 nanoparticles in PMMA. The TEM sample was prepared as following: A single drop of Fe_3O_4 nanoparticles/PMMA solution was placed onto a 400-mesh carbon-coated copper grid using a pipette. Subsequently the sample was dried in air or in the oven. The TEM analysis were performed using a Hitachi H7500 TEM with a magnification up to 200,000x at 100 kV and a resolution up to 1.5 nm. The voltage used in present experiments was 80 kV and the magnification was 60,000 or 120,000x.

5.2.2 Scanning Electron Microscopy

Scanning electron microscopy (SEM) investigation was conducted by a FE-SEM (S4700 Field-Emission SEM, Hitachi) with magnification up to 500,000x and resolution up to 2 nm. Two configurations for SEM were used in the thesis: top-view and cross-section imaging. In the top-view SEM, the sample was glued with carbon tape onto the specimen stage. For the cross-section SEM, the sample was firstly cleaved in order to obtain a fresh cross-section. Subsequently the cleaved sample was clamped on a special sample stage with the sample plane perpendicular to the stage plane. The typical acceleration voltage was in the range of 6 to 8 keV and the working distance is 9 mm approximately.

5.2.3 Alternating Field Gradient Magnetometer

The hysteresis loops of the samples were measured by alternating field gradient magnetometer (AFGM). Before the measurement, a standard Ni foil on glass substrate was used to calibrate the magnetometer. The samples were loaded on two probes which allowed for measurements with magnetic fields parallel or perpendicular to the sample surface. Three measurement configurations with different magnetic field orientations are described in Figure 8.1. During the measurement, the magnetic field varied from -11 kOe to 11 kOe at a step of 250 Oe to magnetize the sample.

5.2.4 Generalized Ellipsometry

Generalized ellipsometry (GE) measurement was conducted with a J. A. Woollam Co., Inc. M-2000VI ellipsometer covering the spectral range from 370 nm to 1700 nm (0.73 eV to 3.34 eV) with 590 wavelengthes. An horizontal stage controlled by computer allows for an automated in-plane rotation of the sample. A goniometer is utilized to control the angle of incidence. The Mueller matrix elements normalized to M_{11}, except for the fourth row of elements from M_{41} to M_{44}, can be measured by this equipment.

The Mueller matrix element measurement was performed in a spectral range from 400 nm to 1700 nm. The angle of incidence Φ_a varied from 45° to 75° at a step of 10° and the in-plane rotation angle ϕ (sample azimuth) of the sample was shifted from 0° to 360° at a step of 6°. The measurements on the SCTFs and SCTF composites were performed by initially placing the sample on the rotation stage such that the slanted nanocolumns on the sample pointed towards the light source of the ellipsometer and parallelled the plane of incidence. After the measurement, the data analysis was performed with the use of software WVASE32.

5.2.5 Vector Magneto-Optical Generalized Ellipsometry

A vector magneto-optical generalized ellipsometer is composed of a V-VASE ellipsometer and an octupole vector-magnet installed on the V-VASE goniometer. The V-VASE ellipsometer is capable of measuring within a spectral range from 0.75 eV to 5.5 eV. The automated sample stage is installed vertically such that the stage plane is perpendicular to the optical table. Two focusing probes are attached to the ellipsometer so that the light beam can be focused into a much

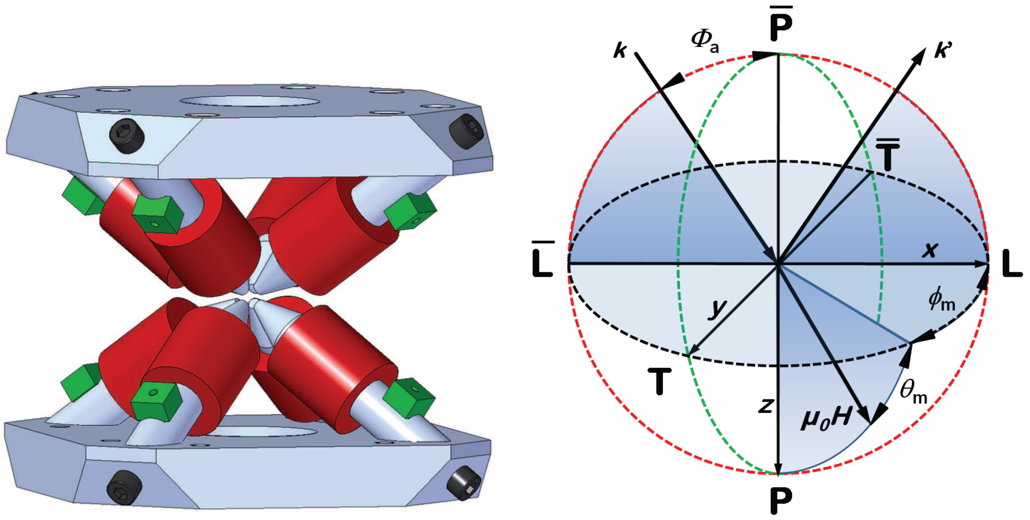

(a) (b)

Figure 5.1: (a) Scheme of the vector-magnet with four solenoid pairs; (b) illustration of the Cartesian coordinate system (x,y,z) for the VMOGE. **k** and **k**' denote the incident and reflected wave vectors respectively, with an angle of incidence Φ_a. The orientation of the external magnetic field $\mu_0\mathbf{H}$ is defined by the azimuth ϕ_m and polar angle θ_m. P, L and T correspond to the measurement with magnetic field in the laboratory coordinate directions x, y and z respectively while $\bar{P}$, $\bar{L}$ and $\bar{T}$ denote the directions -x, -y and -z. Schemes adapted from(44).

smaller spot. The Mueller matrix elements normalized to M_{11}, except for the fourth row of elements, can be measured by this equipment.

The octupole vector-magnet is comprised of four solenoid pairs as illustrated in Figure 5.1a. Each solenoid pair can generate a magnetic field along the diagonal direction of a cube and the overall magnetic field is the vector addition of the three diagonal magnetic field components. The current through the solenoid pairs can be adjusted by four power supplies such that the magnitude and direction of the overall field can be adjusted by controlling the currents through each solenoid. The Cartesian coordinate system (x,y,z) for the VMOGE is shown in Figure 5.1b. The plane of incidence is within the x-y plane. The magnetic field $\mu_0\mathbf{H} = \mu_0(H_x, H_y, H_z)$ is defined in a spherical coordinate. The orientation of the field is determined by the azimuth angle ϕ_m in x-y plane and the polar angle θ_m. The polar measurement was conducted by simply setting $(H_x = 0, H_y = 0, H_z \neq 0)$. Three major loop scans along LP (longitudinal-polar), LT (longitudinal-transverse) and TP (transverse-polar) were designed. For example, the LP loop is defined such that $\phi_m = 0$ and θ_m changes from 0° to 360°; LT is defined such that ϕ_m changes from 0° to 360° and $\theta_m = 0$; TP loop is defined such that $\phi_m = 90^\circ$ and θ_m changes from 0° to 360°. During loop scans, the direction of $\mu_0\mathbf{H}$ rotates along the LP, LT and TP loops while the magnitude is maintained.

During the measurement, the sample was placed at the center of the vector-magnet while the light beam struck on the sample surface center precisely. Before each VMOGE measurement, a measurement from 400 nm to 1000 nm with $\mathbf{H} = 0$ was performed to determine the in-plane orientation of the sample. In the polar measurement, the Mueller matrix element measurement was performed in a spectral range from 400 nm to 1000 nm with the magnetic field ($\mu_0 H = 0.2\ T$) along +z and -z directions respectively. The experimental data were expressed as difference of Mueller matrix elements between +z and -z field measurements:

$$\Delta M_{k,l} = M_{k,l}(\mu_0 H = 0.2\ T) - M_{k,l}(\mu_0 H = -0.2\ T). \tag{5.1}$$

Loop scan measurements have been performed at a fixed wavelength of 500 nm with a magnetic field ($\mu_0 H = 0.17\ T$). The magnetic field with magnitude 0.17 T was rotated along LP, LT and TP loops from 0° to 360° at a step of 6°. At each rotation interval, a Mueller matrix element measurement was performed. The loop measurement data were extracted as follows:

$$\Delta M_{k,l} = M_{k,l}(\mu_0 H = 0.17\ T) - M_{k,l}(\mu_0 H = 0\ T), \tag{5.2}$$

and presented as a function of rotation angle.

Chapter 6

The Dispersion of Fe_3O_4 Nanoparticles in PMMA

The dispersion of nanoparticles in a polymer matrix is crucial for the performance of the composites. However, due to the van der Waals force and the magnetic force the magnetic nanoparticles tend to aggregate to form clusters, and it becomes a challenge to reach a uniform distribution of nanoparticles in a polymer matrix. The common methods for nanoparticle dispersion include chemical reaction and physical blending. The chemical reaction route often involves complicated and tedious procedure. In this chapter, a simple physical blending process was used to achieve a uniform dispersion of Fe_3O_4 nanoparticles in PMMA. The preparation conditions such as nanoparticle concentration and drying process were varied to optimize the dispersion. Transmission electron microscopy (TEM) and scanning electron microscopy (SEM) were used to investigate the dispersion of the nanoparticles in the PMMA matrix. The Fe_3O_4/PMMA solution and TEM samples were prepared by the method described in Section 5.1.2 and Section 5.2.1.

6.1 TEM Analysis

Figure 6.1 shows the TEM image of the samples with different nanoparticle concentrations in PMMA. As indicated in the images, the aggregation increases with nanoparticle concentration. The sample with 1 wt% nanoparticle concentration

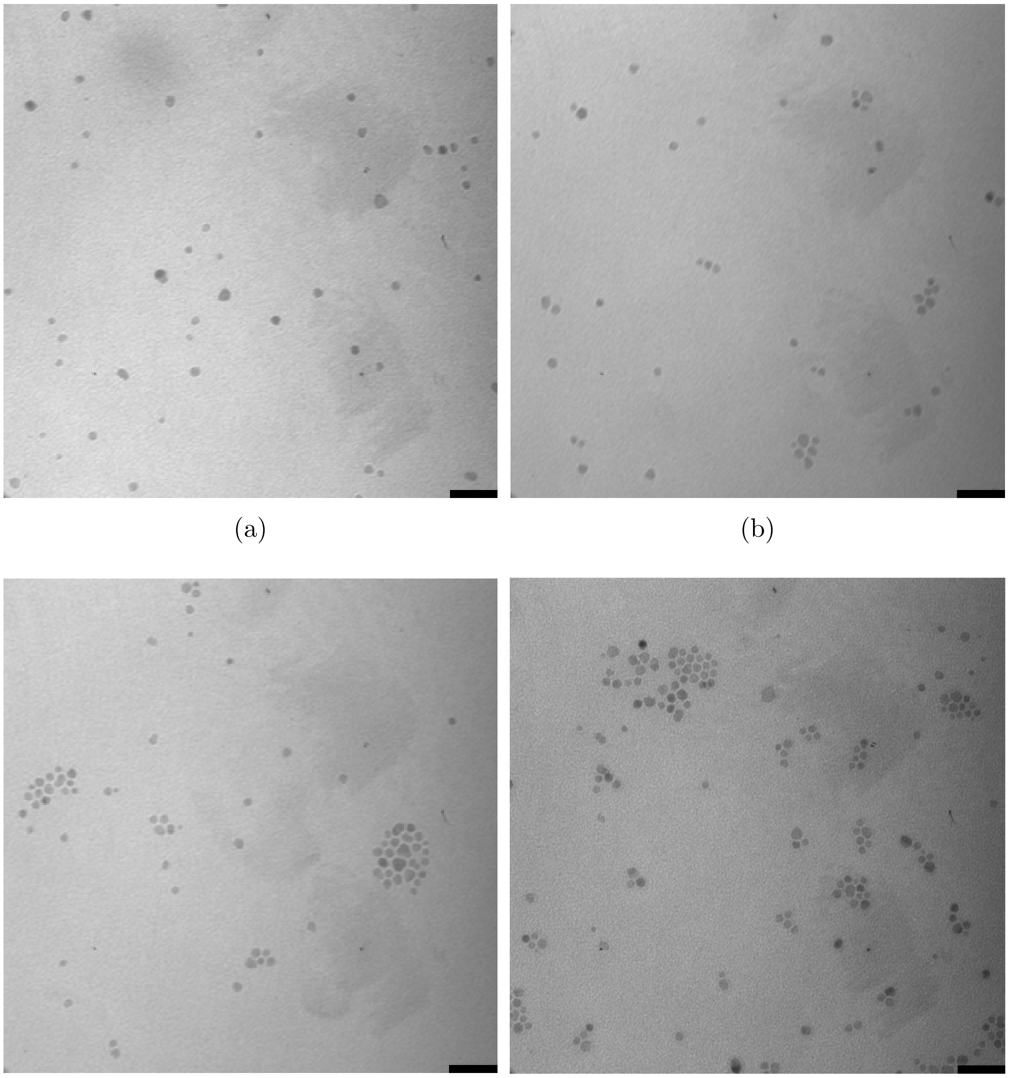

(a) (b)

(c) (d)

Figure 6.1: TEM image of Fe_3O_4 nanoparticles with different concentrations dipersed in PMMA: (a) 1 wt%; (b) 2 wt%; (c) 3 wt%; (d) 5 wt%. All samples were dried at 50 °C for 22 h. Scale bar: 50 nm.

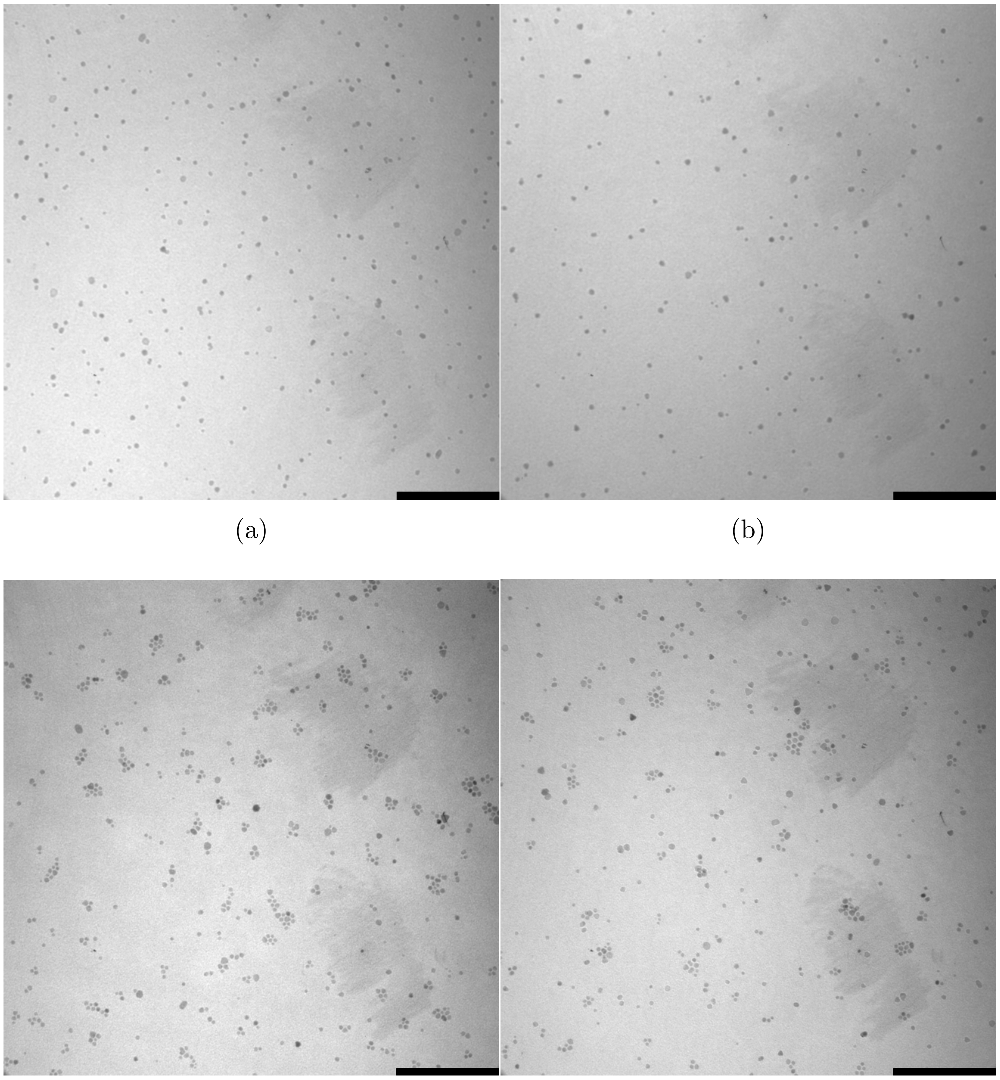

(a) (b) (c) (d)

Figure 6.2: TEM images of Fe_3O_4 nanoparticles in PMMA dried at different conditions: (a) 1 wt% nanoparticles in PMMA dried at room temperature; (b) 1 wt% nanoparticles in PMMA dried at 100 °C for 22 h; (c) 5 wt% nanoparticles in PMMA dried in air; (d) 5 wt% nanoparticles in PMMA dried at 100 °C for 1 h. Scale bar: 200 nm.

shows the best dispersion. For the composites prepared by sonication blending, PMMA is physically adsorbed at the magnetic nanoparticle surface, which creates steric repulsion force to balance the magnetic and van der Waals attractive forces of the nanoparticles and consequently separates the nanoparticles(52) from each other. However as the nanoparticle concentration increases, the nanoparticles have higher chance to contact mutually without polymer coating, therefore more aggregations occur with higher nanoparticle concentration.

TEM images of 1 wt% and 5 wt% Fe_3O_4 nanoparticles in PMMA dried at different conditions are displayed in Figure 6.2. At both nanoparticle concentrations, heat treatment above T_g of PMMA caused no further agglomeration in the sample. Thus, it is concluded that the nanoparticle dispersion in PMMA can be still maintained by drying the sample at 100 °C.

6.2 SEM Analysis

The dispersion of Fe_3O_4 nanoparticles in PMMA can also be observed by SEM as shown in Figure 6.3. Before using SEM, the Fe_3O_4 nanoparticles/PMMA composites were spin-coated on Si substrates to form a thin film. For spin-coated samples, the dispersion of the nanoparticles shows similar patterns as observed in Figure 6.1. The dark background corresponds to the PMMA matrix. The bright spots in Figure 6.3a represents the well-distributed nanoparticles in PMMA matrix. The bright clusters in Figure 6.3b correspond to the nanoparticle aggregations in the sample with 5 wt% of nanoparticles.

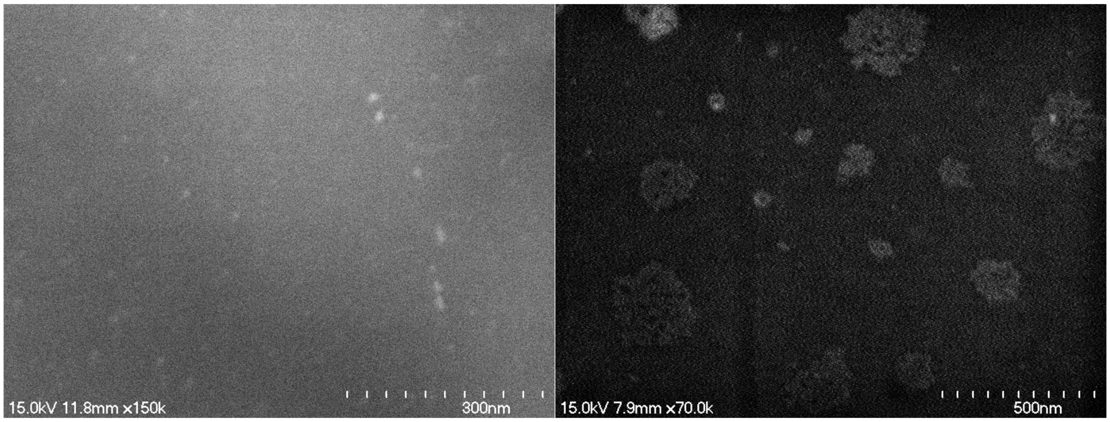

(a) (b)

Figure 6.3: SEM images of Fe_3O_4 nanoparticles/PMMA spin-coated on Si substrate: (a) 1 wt%; (b) 5 wt%.

6.3 Summary

In conclusion, the best uniform dispersion of nanoparticles in PMMA matrix is achieved in the sample with 1 wt% nanoparticles. The nanoparticle concentration in PMMA is an important factor for nanoparticle aggregation while drying samples at 100 °C does not change the dispersion radically. SEM images also indicate that the agglomeration increases in the polymer matrix as nanoparticle concentration enhances.

Chapter 7

Structural and Optical Properties of SCTF Composites

7.1 Structural Property

The optical constants of PMMA and 5 wt% Fe_3O_4 nanoparticles/PMMA composites (5 wt% Fe_3O_4 nanoparticles/PMMA) were determined by ellipsometry analysis before the analysis of FeNi SCTFs infiltrated with PMMA and 5 wt% Fe_3O_4 nanoparticles/PMMA (SCTF composites). PMMA and 5 wt% Fe_3O_4 nanoparticles/PMMA were spin-coated on the Si substrates respectively. After dried in air, the samples were measured by M-2000VI ellipsometer. A Cauchy model was used to fit the experimental data since the samples are transparent with only a small absorption in the spectral range from 400 nm to 1700 nm. The optical constants obtained from the best-match model are shown in Figure 7.1. As seen from Figure 7.1, a slight difference in refractive index exists between PMMA and 5 wt% Fe_3O_4 nanoparticles/PMMA.

The optical model used to analyze the experimental data of SCTF composites is shown schematically in Figure 7.2. A monoclinic biaxial layer (described in Section 4.3.3) was built on top of the Si substrate to model FeNi SCTFs. The AB-EMA (discussed in Section 4.3.5) was applied to model the optical constants of the monoclinic layer along the three major polarizability axes **a**, **b** and **c**. The **c** axis is chosen to be along the pointing direction of the slanted nanocolumns.

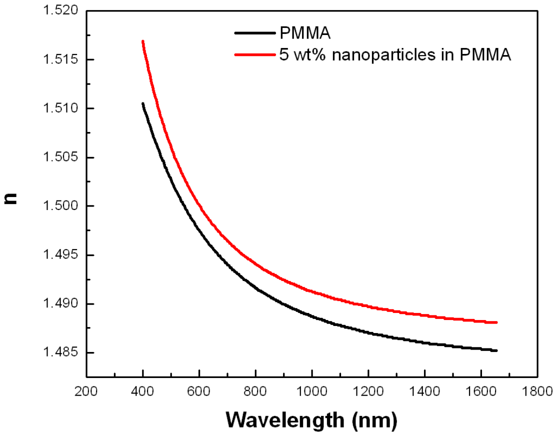

Figure 7.1: The optical constants of PMMA and 5 wt% Fe_3O_4 nanoparticles/PMMA composites.

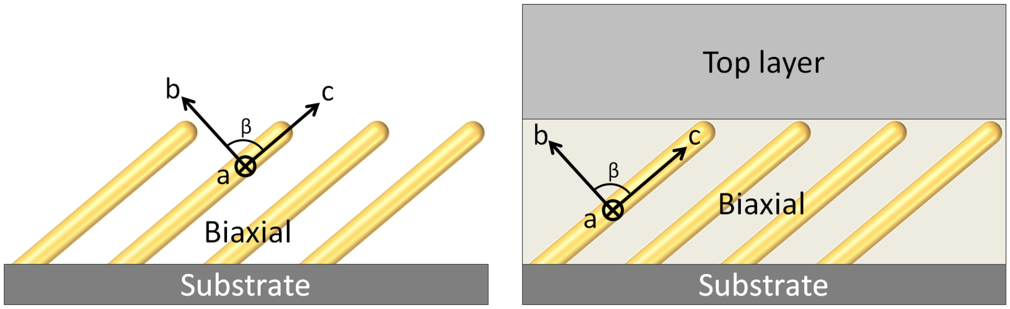

(a) (b)

Figure 7.2: Optical Model for (a) FeNi SCTFs, (b) FeNi SCTFs infiltrated with PMMA or 5 wt% Fe_3O_4 nanoparticles/PMMA. **a**, **b** and **c** denote the major polarizability axes, β is the internal angle between **b** and **c**.

The other two axes **a** and **b** are perpendicular to the nanocolumns and **a** is also parallel to the substrate surface. Thus, the internal angles α and γ were fixed at 90° while the angle β between the axes **b** and **c** is a modeling parameter. The three Euler angles φ, θ and ψ which transform the Cartesian coordinate system (x, y, z) to the major polarizability axis system (a, b, b) were the parameters to determine the orientation of the anisotropic sample (discussed in Section 4.3.3). The two-phase AB-EMA for FeNi SCTFs are comprised of FeNi and voids.

In the model for FeNi SCTFs infiltrated with PMMA or with 5 wt% $\mathrm{Fe_3O_4}$ nanoparticles/PMMA, an orthorhombic biaxial layer (described in Section 4.3.3) was built above the Si substrate and a top layer was used to model the outstanding material above the FeNi SCTF after spin-coating. The AB-EMA was applied to model the optical constants of the orthorhombic biaxial layer along the three major polarizability axes **a**, **b** and **c**. The arrangement of the three major axes was similar to that for FeNi SCTFs except that the internal angles α, β and γ were assumed to be 90° since the orthorhombic biaxial model was used. The three Euler angles φ, θ and ψ were the modeling parameters to determine the orientation of the anisotropic sample. The three-phase AB-EMA for FeNi SCTF composites consists of FeNi, infiltration materials and void. During the modeling, the parameters such as biaxial layer thickness, the Euler angle θ and FeNi void fraction were coupled such that these parameters are the same for both infiltrated samples.

For all the samples, the depolarization factors L_a^D, L_b^D, L_c^D are utilized to model the biaxial effective dielectric functions.

The best-match model results are summarized in Table 7.1. From the results, the difference in some parameters reflects the structural change of the SCTFs after infiltration. First, it is noted that the thickness of the biaxial layer decreased from 86.4 to 73.9 nm and the Euler angle θ increased from 63.57 to 72.46° by almost 10°. θ represents the acute angle between the major axis **c** (along the pointing direction of the slanted nanocolumns) and the Cartesian laboratory axis z (normal to the substrate surface). Thus the increasing θ indicates that after infiltration the slanted nanocolumns were approximately 10° more inclined to the substrate surface. This incline also resulted in the decrease of the biaxial layer thickness from 86.4 to 73.9 nm. Secondly, the results show that a top layer which is about 60 nm is above the biaxial layer, which could be the cause of the more inclined nanocolumns after infiltration. The void fractions declined greatly from 74.87% to 5.32% and 8.74% after infiltration, which proves an excellent material infiltration into the void of FeNi SCTFs. The smaller void fraction reveals a better infiltration with PMMA than 5 wt% Fe_3O_4 nanoparticles/PMMA. The depolarization factors generally follow the order $L_b^D > L_a^D > L_c^D$. The depolarization factor L_c^D smaller than the other two illuminates that the structure extends in the c-axis which is along the pointing direction of the nanocolumns, but $L_c^D \neq 0$ reflects the fact that the nanocolumns is not infinitely long. Due to the material infiltration, L_c^D shows a noticeable increase after infiltration while L_a^D decreases appreciably.

Table 7.1: The Best-match model results of AB-EMA for FeNi SCTFs, FeNi SCTFs infiltrated with PMMA (SCTF/PMMA), FeNi SCTFs infiltrated with 5 wt% Fe_3O_4 nanoparticles/PMMA (SCTF/PMMA/NP). * denotes the coupled parameters in the modeling. The error limits given in parentheses denote the uncertainty of the last digit.

Parameter	SCTFs	SCTF/PMMA	SCTF/PMMA/NP
Biaxial layer thickness (nm)	86.4(1)	73.9(1)*	73.9(1)*
Top layer thickness (nm)	NA	58.97(9)	64.04(8)
φ (°)	95.36(1)	96.56(1)	3.65(1)
θ (°)	63.57(3)	72.76(4)*	72.76(4)*
β (°)	82.43(8)	90 (fixed)	90 (fixed)
FeNi fraction (%)	25.13	25.09(4)*	25.09(4)*
Void fraction (%)	74.87(3)	5.32	8.74
Infiltration fraction (%)	NA	69.6(2)	66.2(2)
L_c^D	0.1128(9)	0.1344(9)	0.1448(9)
L_a^D	0.393	0.3694	0.366
L_b^D	0.4943	0.4962	0.4893
MSE	11.72	5.32	5.32

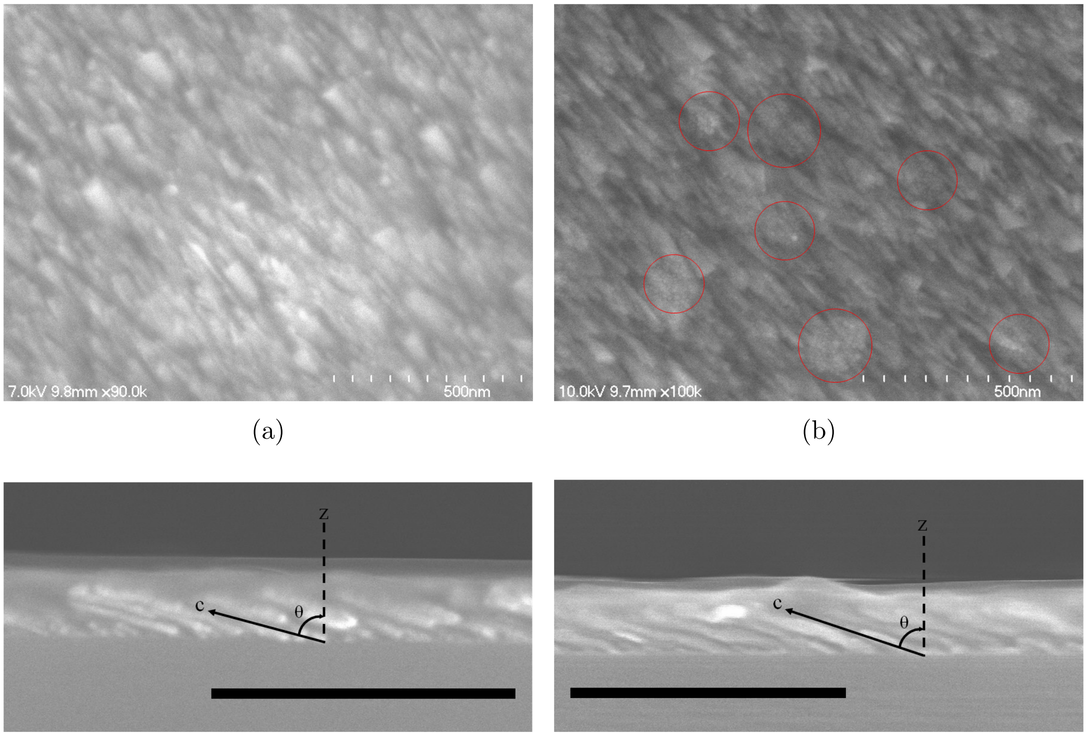

(a) (b)

(c) (d)

Figure 7.3: The SEM images of the FeNi SCTF composites: (a) the top-view of FeNi SCTFs infiltrated with PMMA; (b) the top-view of FeNi SCTFs infiltrated with 5 wt% Fe_3O_4 nanoparticles/PMMA; (c) the cross-section of FeNi SCTFs infiltrated with PMMA; (d) the cross-section of FeNi SCTFs infiltrated with 5 wt% Fe_3O_4 nanoparticles/PMMA. The red circles in (b) indicate the areas where the nanoparticle clusters exist. θ in (c) and (d) represents the angle between the c axis (along the pointing direction of the slanted nanocolumns) and the Cartesian laboratory axis z (normal to the substrate surface). The scale bars in (c) and (d) are 500 nm.

The top-view and cross-section SEM images of the FeNi SCTF composites are displayed in Figure 7.3. In the top-view SEM, the images of the the slanted nanocolumns are blurred because of the top layer. From Figure 7.3b, the nanoparticle clusters in the top composite layer can be seen. Even though the separated nanoparticles can not be observed in this image because of the resolution limit, it is deduced that they are distributed in the top layer and also infiltrated into the void of the SCTFs. In the cross-section SEM, PMMA or 5 wt% Fe_3O_4 nanoparticles/PMMA penetrated to the interspace of the nanocolumns filling the void completely, which indicates an excellent infiltration. The top layer can be clearly observed in the cross-section images. The structural parameters of the samples evaluated by SEM are summarized in Table 7.2 and compared with the results acquired by GE analysis. The thickness results obtained by SEM and GE are very consistent and the SEM analysis also indicates that $\theta = 73°$ approximately for the FeNi SCTF composites.

Table 7.2: Summary of the structural parameters of FeNi SCTFs infiltrated with PMMA (SCTF/PMMA) and FeNi SCTFs infiltrated with 5 wt% Fe_3O_4 nanoparticles/PMMA (SCTF/PMMA/NP) obtained by GE and SEM analysis. The error limits given in parentheses denote the uncertainty of the last digit in the GE analysis.

	SCTF/PMMA		SCTF/PMMA/NP	
	GE	SEM	GE	SEM
Biaxial layer thickness (nm)	73.9(1)	76.1	73.9(1)	68.2
Top layer thickness (nm)	58.97(9)	60.1	64.04(8)	66.3
θ (°)	72.76(4)	74.1	72.76(4)	71.9

7.2 Optical Property

Figure 7.4 shows the experimental and best-model calculated Mueller matrix elements versus sample azimuth ϕ and angle of incidence Φ_a at wavelength $\lambda = 601$

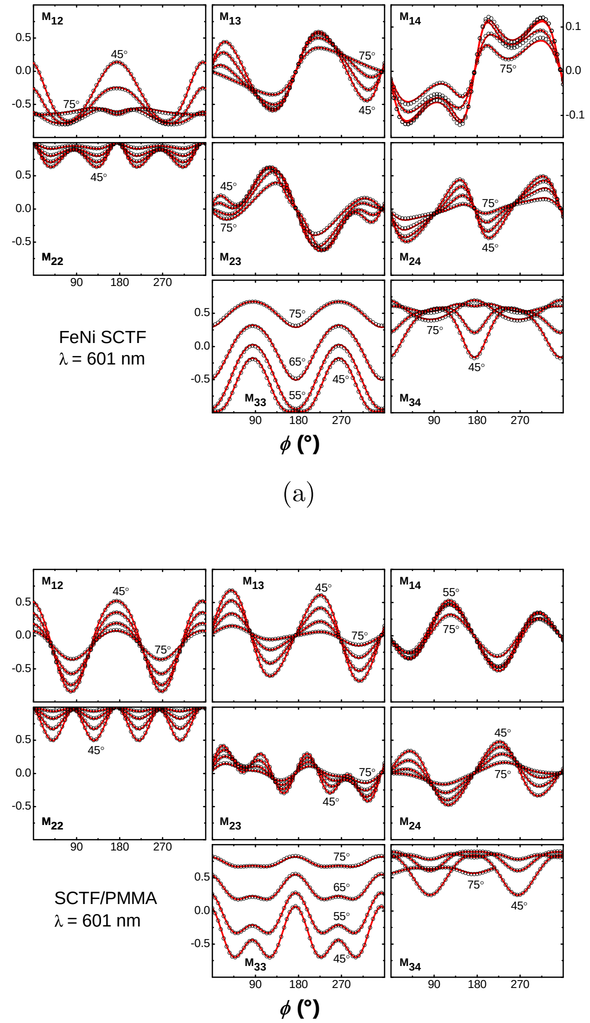

(a)

(b)

Figure 7.4: Experimental (open circle) and best-match calculated (solid line) GE data versus sample azimuth ϕ and angle of incidence $\Phi_a = 45°, 55°, 65°, 75°$ at $\lambda = 601$ nm: (a) FeNi SCTFs; (b) FeNi SCTFs infiltrated with PMMA. The GE data are presented by Mueller matrix elements M_{ij} normalized to M_{11}. Note that in (a) the scale of the vertical ordinate of M_{14} is different from the rest of the Mueller matrix elements.

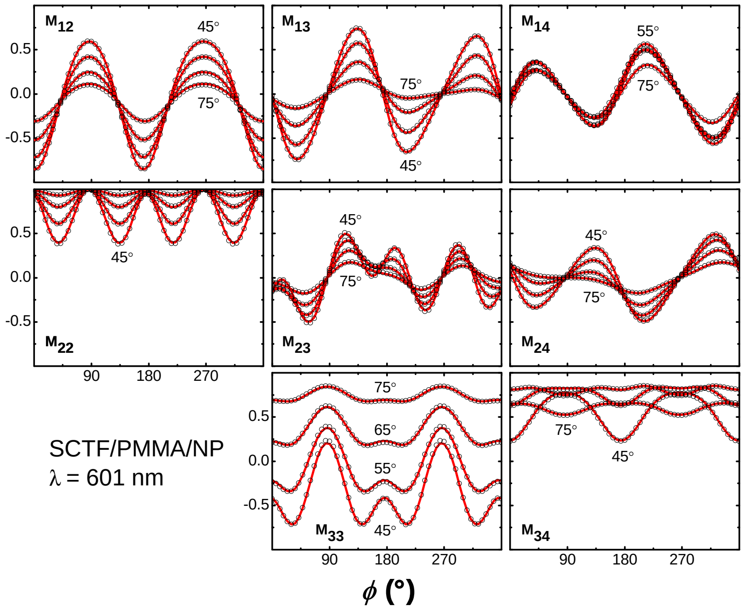

Figure 7.5: Experimental (open circle) and best-match calculated (solid line) GE data of FeNi SCTFs infiltrated with 5 wt% Fe_3O_4 nanoparticles/PMMA versus sample azimuth ϕ and angle of incidence $\Phi_a = 45°, 55°, 65°, 75°$ at $\lambda = 601$ nm. The GE data are presented by Mueller matrix elements M_{ij} normalized to M_{11}.

nm for FeNi SCTFs and FeNi SCTFs infiltrated with PMMA. The Mueller matrix elements which are not shown in the figure can be obtained by symmetry(40). The experimental and best-match calculated data exhibit excellence fit for both samples. The off-diagonal elements including M_{13}, M_{14}, M_{23} and M_{24} for both samples show a variation versus sample azimuth ϕ and a two-fold rotational symmetry, which reveals a strong optical anisotropy in the materials since these elements are zero for isotropic samples regardless of sample azimuth, angle of incidence and wavelength(42). The off-diagonal elements approach to zero for all angles of incidence and wavelengthes at $\phi \approx 0°$ and $180°$ where the tilting direction of the nanocolumns is parallel to the plane of incidence. This phenomenon is termed the pseudo-isotropic sample orientation(42). Comparing the off-diagonal elements of the two samples, the variation patterns change after PMMA infiltration while the two-fold symmetry is maintained. It is observed that the intensity of M_{14} is enhanced greatly after PMMA infiltration.

The exemplary Mueller matrix elements versus sample azimuth ϕ and angle of incidence at $\lambda = 601$ nm for FeNi SCTFs infiltrated with 5 wt% Fe_3O_4 nanoparticles/PMMA are shown in Figure 7.5. From the modeling results, it is obtained that the Euler angle $\varphi = 3°$ which corresponds to the configuration that the nanocolumns point towards the -y direction in the laboratory coordinate system. This explains that the Mueller matrix element pattern is shifted 90° to the right compared with that of the former two samples. Nevertheless, the Mueller matrix element data of the two SCTF composites shows no difference.

The optical constants of the biaxial layer versus wavelength obtained by modeling are exhibited in Figure 7.6. The biaxial layers of all three samples show strong birefringence and dichroism. The wavelength dispersion of the optical constants for FeNi SCTF composites follows the similar pattern as that for FeNi SCTFs. The refractive index n_c and extinction coefficient k_c along **c** axis have the strongest wavelength dispersion compared with the optical constants along **a** and **b**. For all three samples, n_c crosses n_a and n_b in the middle of the spectra and $k_c > k_a > k_b$. Nevertheless, the optical constants of the FeNi SCTF composites show great difference from that of FeNi SCTFs. Due to the excellent material infiltration into the voids of SCTFs, the refractive index n and extinction coefficient k along all the axes have enhanced greatly across the investigated spectral range. Whereas the optical constants for the two infiltrated samples are found to be similar. The slight distinction may be cause by different void fractions and the difference in optical constants between the two infiltration materials.

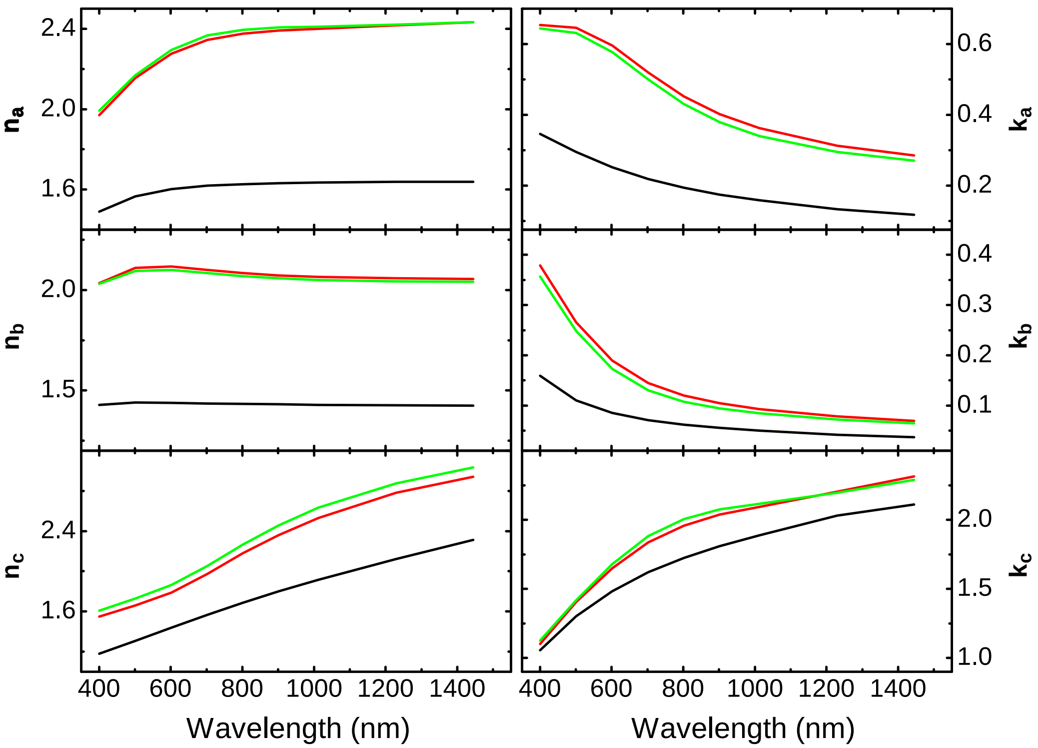

Figure 7.6: Optical constants for the biaxial layers of FeNi SCTFs (black line), FeNi SCTFs infiltrated with PMMA (red line) and SCTFs infiltrated with 5 wt% Fe_3O_4 nanoparticles/PMMA (green line) along the major axes **a**, **b** and **c**: n_a, n_b, n_c and k_a, k_b, k_c.

7.3 Summary

GE was employed to characterize the structural and optical properties of FeNi SCTFs infiltrated with PMMA and 5 wt% Fe_3O_4 nanoparticles/PMMA. AB-EMA was used to model the GE data. The results show that the samples possess a biaxial structure with the c axis along the pointing direction of the nanocolumns. The structural parameters obtained by modeling are consistent with those of the SEM analysis, which indicates that after infiltration the infiltrated samples possess a top layer above the slanted nanocolumns and the nanocolumns were approximately 10° more inclined to the substrate surface. The low void fraction reveals that an excellent infiltration was achieved. The GE analysis reflects that all the samples have a strong optical anisotropy. Due to the excellent material infiltration into the void of SCTFs, the optical constants along the three major axes have enhanced greatly across the investigated spectral range.

Chapter 8

Magnetic Properties of SCTF Composites

8.1 Magnetic Hysteresis Loop Measurement

Magnetic hysteresis loops of the SCTF composites measured by AGFM are exhibited in Figure 8.1 and the obtained magnetic parameters are summarized in Table 8.1. The measurement of 5 wt% Fe_3O_4 nanoparticles/PMMA spin-coated on Si substrate by AGFM was unsuccessful because the sensitivity of the AFGM was not able to detect the magnetic response of the nanoparticles at such a low amount. The different shapes of the hysteresis loops reveal the strong magnetic anisotropy of the samples. As shown in Figure 8.1a, with an external magnetic field **H** perpendicular ($\perp$) to the **a** axis and parallel ($\|$) to the substrate surface, the SCTF composites reached the saturation magnetization at a lower field compared with the other two configurations shown in Figure 8.1b and 8.1c. According to Table 8.1, both coercivity and remanence in Figure 8.1a show the greatest values compared with the other two configurations. This result indicates that the easier magnetization occurred with $\mathbf{H} \perp \mathbf{a}$ and $\|$ substrate surface.

In Table 8.1, the magnetic parameters of the two SCTF composite samples are appreciably different. Since the magnetic measurement of the SCTFs are very sensitive to the sample orientation(23,24), the variations on the parameters can be explained by the sample orientation errors in separated measurements.

Table 8.1: Coercivity (H_c) and remanence magnetization normalized to the saturation magnetization (M_r/M_s) of FeNi SCTFs infiltrated with PMMA (SCTF/PMMA) and FeNi SCTFs infiltrated with 5 wt% Fe_3O_4 nanoparticles/PMMA (SCTF/PMMA/NP) measured by AGFM. (a), (b) and (c) correspond to the same measurement configurations in Figure 8.1a, 8.1b and 8.1c respectively.

	SCTF/PMMA			SCTF/PMMA/NP		
	(a)	(b)	(c)	(a)	(b)	(c)
H_c (Oe)	647	172	585	671.5	198	509
M_r/M_s	0.78	0.16	0.21	0.86	0.17	0.18

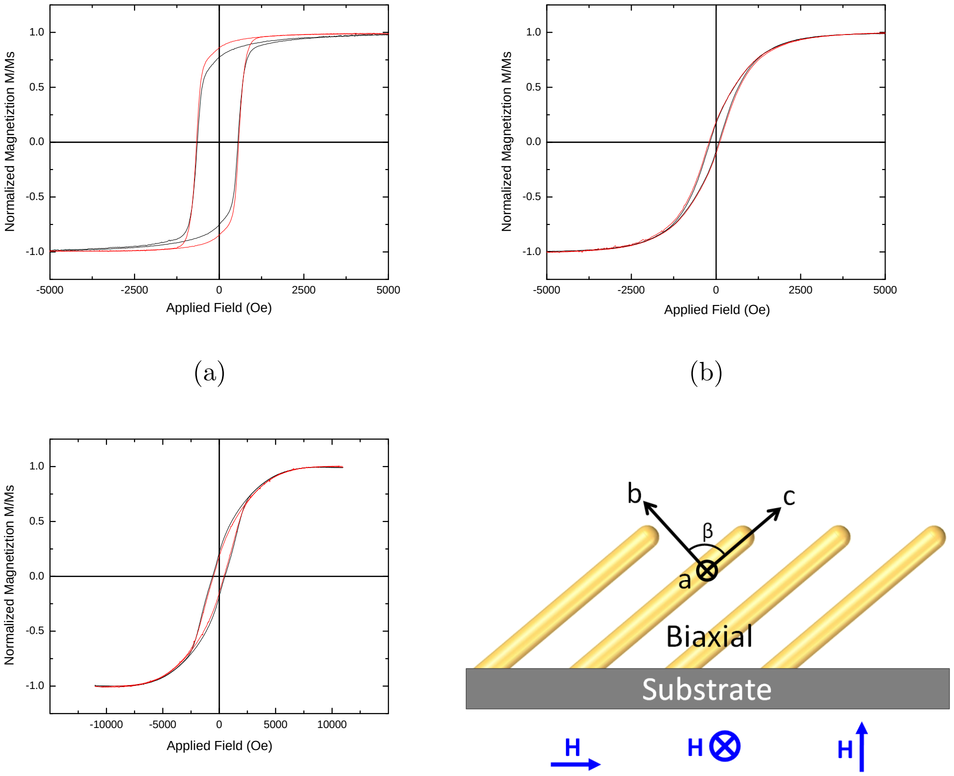

(a)

(b)

(c)

(d)

Figure 8.1: Magnetic hysteresis loops of of FeNi SCTFs infiltrated with PMMA (black solid line) and 5 wt% Fe_3O_4 nanoparticles/PMMA (red solid line) measured with different magnetic field directions: (a) $\mathbf{H} \perp \mathbf{a}$ axis and $\parallel$ substrate surface; (b) $\mathbf{H} \parallel \mathbf{a}$ axis; (c) $\mathbf{H} \perp$ substrate surface; (d) the measurement configurations. **H** is the applied magnetic field. The definition of **a** axis is described in Section 7.1. The magnetization M is normalized to the saturation magnetization M_s. The blue symbols in (d) denote the three different orientations of the magnetic fields **H** used in the corresponding configurations.

8.2 Polar Kerr Effect Generalized Ellipsometry Measurement

The Kerr effect of the SCTF composites was measured in polar configuration as shown in Figure 8.2 with $\Phi_a = 45°$, $\phi = 53°$ approximately, and $\mu_0 H = 0.2\ T$. The external magnetic field was perpendicular to the substrate surface. The Mueller matrix element measurement was performed in a spectral range from 1.24 to 3.1 eV (400 to 1000 nm) without external magnetic field to determine the sample azimuth ϕ. Before the measurement on SCTF composites, the polar Kerr effect measurement was conducted on 5 wt% Fe_3O_4 nanoparticles/PMMA spin-coated on Si substrate. The MO response of Fe_3O_4 nanoparticles embedded in PMMA at such a concentration was found to be within the signal error. Therefore, the present modeling neglected the MO response from the Fe_3O_4 nanoparticles/PMMA layer on the top and only considers that from the infiltrated biaxial layer above the substrate. The structural and optical parameters were adapted from the optical modeling described in Section 7.1 and 7.2. Only the complex magneto-optical (MO) tensor element ε_{xy}^{MO} corresponding to the magnetization direction along the Cartesian laboratory axis $\mathbf{z}$ was determined by matching the calculated and experimental Muellar matrix difference data as described in Equation 5.1. A wavelength-by-wavelength analysis was performed to model the experimental data and determine the complex magneto-optical tensor element ε_{xy}^{MO} versus photon energy.

Figure 8.3 shows the calculated and experimental off-diagonal Muellar matrix element difference data. The calculated and experimental data exhibit a good match for both samples, thus the model scenario which assumes the sample magnetization oriented along the external magnetic field direction in $\mathbf{z}$ represents the experimental fact.

The real and imaginary part of the complex magneto-optical tensor element ε_{xy}^{MO} versus photon energy was plotted in Figure 8.4 by wavelength-by-wavelength analysis. The symbols represent the obtained tensor element ε_{xy}^{MO} as a function of wavelength. In the polar Kerr effect measurement, ε_{xy}^{MO} is almost identical for both SCTF composite samples, therefore the magnetic nanoparticles have limited

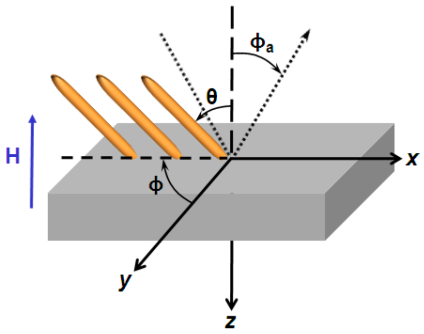

Figure 8.2: The polar measurement configuration with sample azimuth ϕ, column tilt angle θ and angle of incidence Φ_a.

influence on the MO response of SCTFs with this particular field orientation. In order to identify the effect of the nanoparticles on SCTFs, an ellipsometry measurement with magnetic field in arbitrary orientation is required.

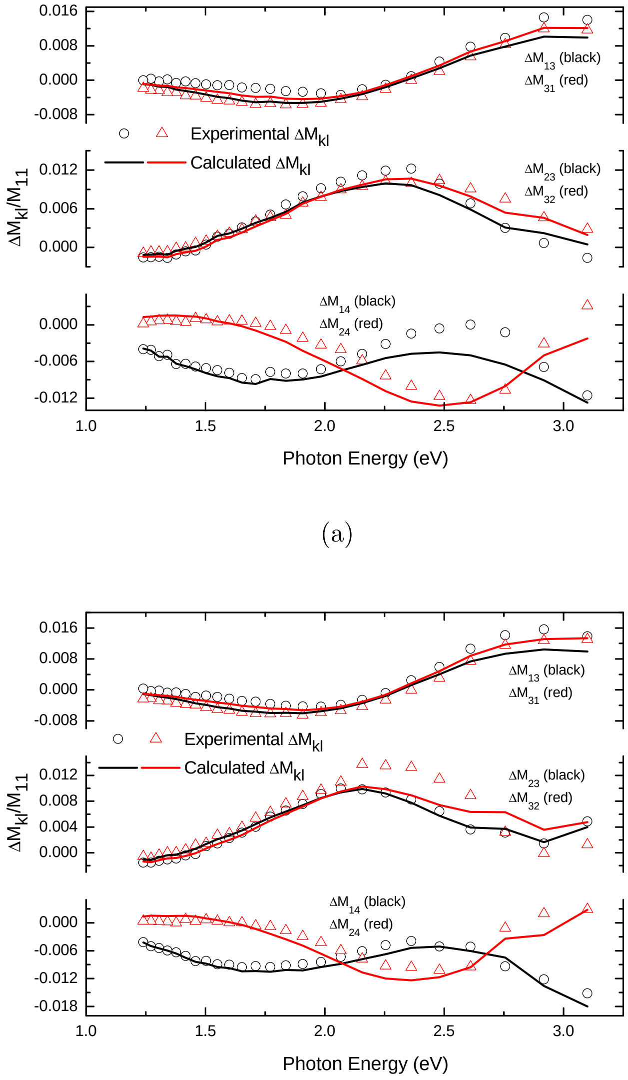

(a)

(b)

Figure 8.3: The calculated and experimental off-diagonal Muellar matrix element difference data $\Delta M_{k,l} = M_{k,l}(\mu_0 H = 0.2\ T) - M_{k,l}(\mu_0 H = -0.2\ T)$ normalized to M_{11} for the SCTF composites: (a) FeNi SCTFs infiltrated with PMMA ($\Phi_a = 45°$, $\phi = 53.5°$); (b)FeNi SCTFs infiltrated with 5 wt% Fe_3O_4 nanoparticles/PMMA ($\Phi_a = 45°$, $\phi = 52.1°$).

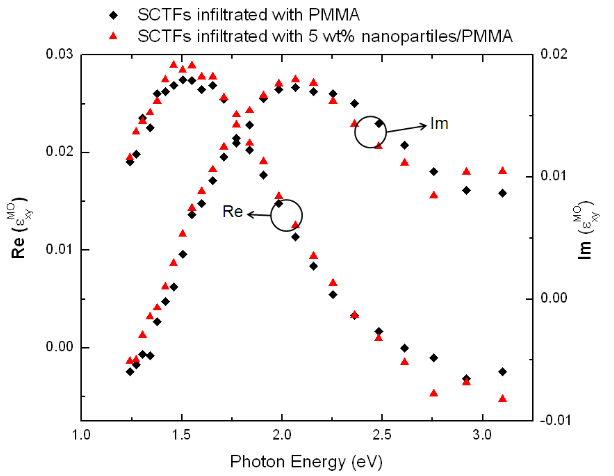

Figure 8.4: The real and imaginary part of the complex magneto-optical tensor element ε_{xy}^{MO} versus photon energy obtained by wavelength-by-wavelength analysis on: FeNi SCTFs infiltrated with PMMA (black diamond) and FeNi SCTFs infiltrated with 5 wt% Fe_3O_4 nanoparticles/PMMA (red triangle).

8.3 Vector Magneto-Optical Generalized Ellipsometry Measurement

In this section, the SCTF composites were measured wia vector magneto-optical generalized ellipsometry (VMOGE) and the three off-diagonal elements of the complex magneto-optical tensor element ε_{xy}^{P}, ε_{xz}^{T} and ε_{yz}^{L} (discussed in Section 4.3.7) were plotted in a 3-dimension coordinate system. Before performing VMOGE measurement, the Mueller matrix element measurement in the spectral range from 400 to 1000 nm without external magnetic field was conducted to determine the sample azimuth ϕ. A zero-field measurement at a single wavelength 500 nm was also performed. The VMOGE measurement details are described in Section 5.2.5. Figure 8.5 illustrates the measurement configuration. Three loop (TP, LT, and PL) measurements were performed at a fixed wavelength of 500 nm with $\Phi_a = 55°$, $\phi = 90°$ approximately and $\mu_0 H = 0.17\ T$. The experimental data was acquired in the form of $\Delta M_{k,l} = M_{k,l}(\mu_0 H = 0.17\ T) - M_{k,l}(\mu_0 H = 0\ T)$ as a function

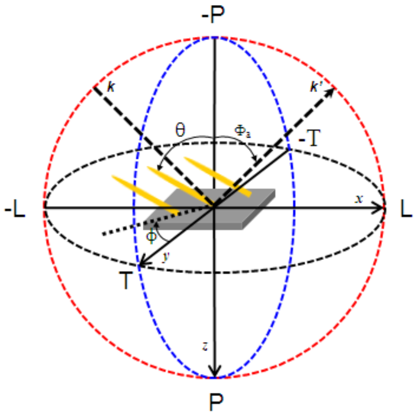

Figure 8.5: The VMOGE measurement configuration with sample azimuth ϕ, column tilt angle θ and angle of incidence Φ_a. P, L and T correspond to the polar, longitudinal and transverse MOKE configurations respectively. The bar over the letters denote the directions -x, -y and -z. **k** and **k**' denote the incident and reflected wave vectors respectively. In the measurement, the direction of external magnetic field $\mu_0 H$ rotates along the LP, LT and TP loops at a step of 6° while the magnitude is maintained. The Mueller matrix element measurement is performed at each magnetic field orientation.

of magnetic field rotation angle ϕ_m and θ_m (described in Section 5.2.5). Before the measurement on SCTF composites, the VMOGE was conducted on 5 wt% Fe_3O_4 nanoparticles/PMMA spin-coated on Si substrate and the MO response of Fe_3O_4 nanoparticles at such a concentration in PMMA was within the signal error. Therefore, the present modeling neglected the MO response from the Fe_3O_4 nanoparticles/PMMA layer on the top and only considers that from the infiltrated biaxial layer above the substrate. In the modeling, the structural and optical parameters were adapted from the optical modeling described in Section 7.1 and 7.2. Only the three complex magneto-optical tensor elements ε_{xy}, ε_{xz} and ε_{yz} were determined by matching the calculated and experimental Muellar matrix difference data. A point-by-point analysis was utilized to model the experimental data and determine the three complex magneto-optical (MO) tensor elements.

The real and imaginary part of the three MO tensor elements (ε_{xy}, ε_{xz} and ε_{yz})

determined by TP, LT and PL loop measurements at wavelength 500 nm on the SCTF composites were plotted in Figure 8.6, 8.7 and 8.8 respectively. The plots of the complex tensor elements generally form elliptical loops in the 3-dimension coordinate. The elliptical loops are obvious for the TP and LT measurements although the ones become less clear for PL measurement. The projection (represented by green symbols) of the loops to ε_{xy}-ε_{yz} plane generally shows an elongated shape with the long axis along the same directions for both samples, which may result from the orientation of the nanocolumns. By the arrows in the figures, the variation of the complex tensor elements can be tracked during each loop measurement. For example, from the real part of the complex tensor element as shown in Figure 8.6b, it is known that the complex tensor elements moved along the loop in the 3-dimension coordinate from T through P and -T to -P. The loop shapes differ in TP, LT, and PL measurements, which indicates the great anisotropic MO property in the SCTF composites. From the figures, it is noted that the loop shapes of the FeNi SCTFs infiltrated with PMMA differ from FeNi SCTFs infiltrated with 5 wt% Fe_3O_4 nanoparticles/PMMA. For instance, from the real part of the complex tensor element as shown in Figure 8.6, it can be noticed that the loop shape for FeNi SCTFs infiltrated with PMMA changes from a column to an ellipse for FeNi SCTFs infiltrated with 5 wt% Fe_3O_4 nanoparticles/PMMA. The loops in the corresponding 2-dimension coordinates also change for the latter sample. For the imaginary part of the complex tensor element as shown in Figure 8.7, the difference in loop shape between the two samples is obvious too. The changes of the loop shapes may be caused by the magnetic Fe_3O_4 nanoparticles which infiltrate into the voids and changes the anisotropy in MO property of the FeNi SCTFs.

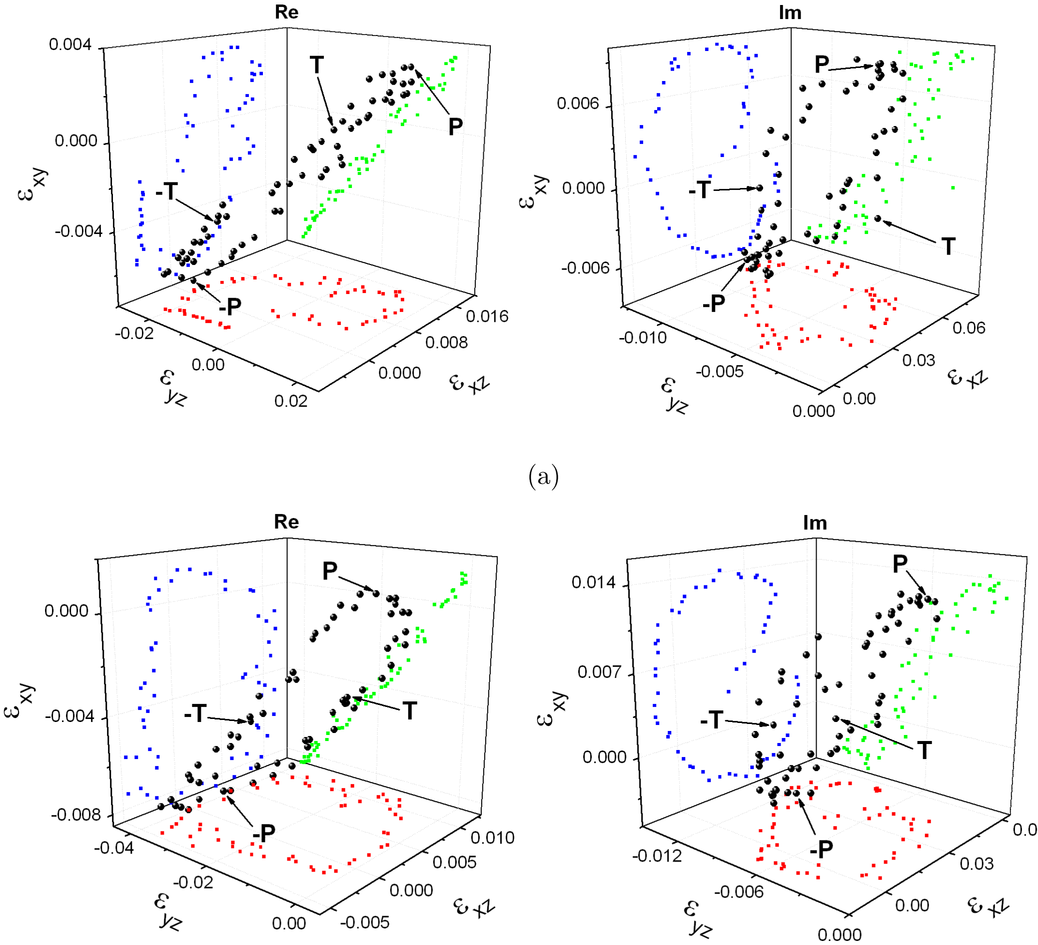

(a)

(b)

Figure 8.6: The magneto-optical tensor elements ε_{xy}, ε_{xz} and ε_{yz} determined by TP loop measurement on the SCTF composites: (a) FeNi SCTFs infiltrated with PMMA ($\phi = 93.9°$); (b)FeNi SCTFs infiltrated with 5 wt% Fe_3O_4 nanoparticles/PMMA ($\phi = 91.6°$). The sphere symbols in black denote the plot of the elements in the 3-dimension coordinate. The square symbols in color denote the plot of the elements in the corresponding 2-dimension coordinates. P, L and T correspond to the measurement with magnetic field in the laboratory coordinate directions x, y and z respectively while -P, -L and -T denote the directions -x, -y and -z. The arrows indicate the elements obtained by P, L, T and -P, -L, -T measurements.

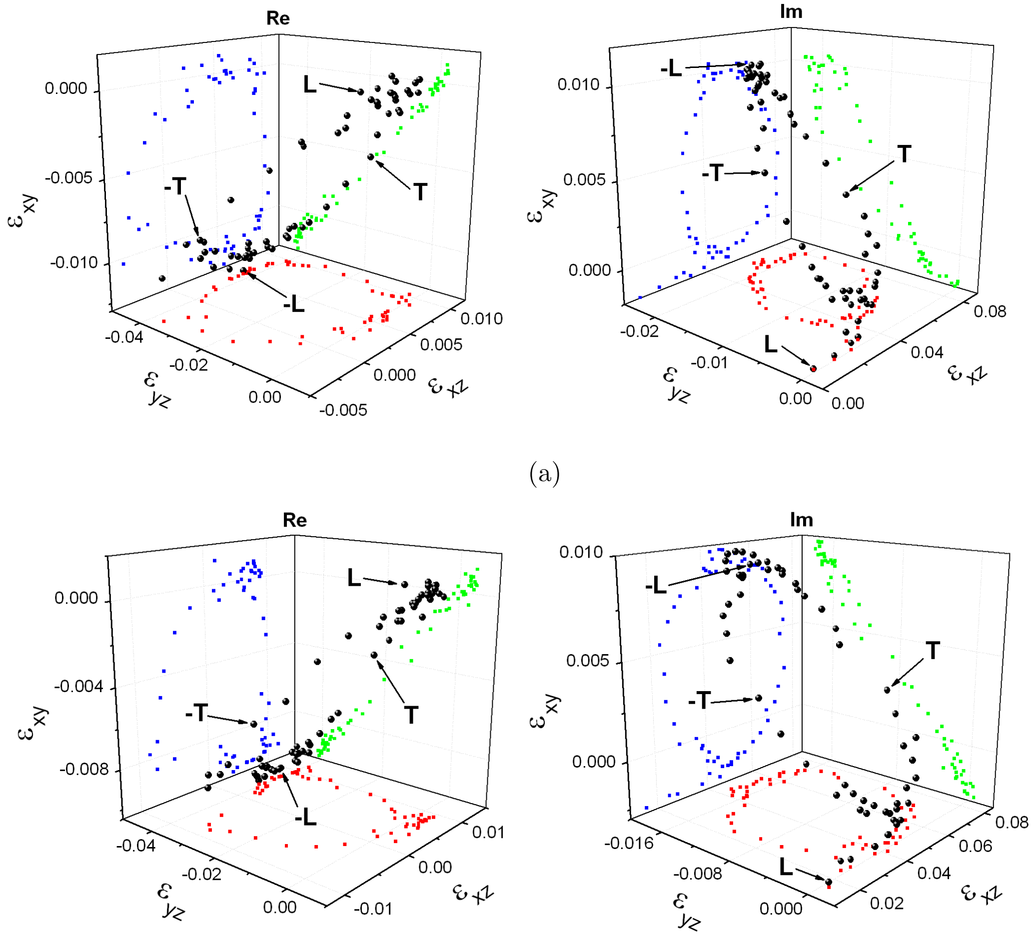

(a)

(b)

Figure 8.7: The magneto-optical tensor elements ε_{xy}, ε_{xz} and ε_{yz} determined by LT loop measurement on the SCTF composites: (a) FeNi SCTFs infiltrated with PMMA ($\phi = 93.9°$); (b)FeNi SCTFs infiltrated with 5 wt% Fe_3O_4 nanoparticles/PMMA ($\phi = 91.6°$). The sphere symbols in black denote the plot of the elements in the 3-dimension coordinate. The square symbols in color denote the plot of the elements in the corresponding 2-dimension coordinates. P, L and T correspond to the measurement with magnetic field in the laboratory coordinate directions x, y and z respectively while -P, -L and -T denote the directions -x, -y and -z. The arrows indicate the elements obtained by P, L, T and -P, -L, -T measurements.

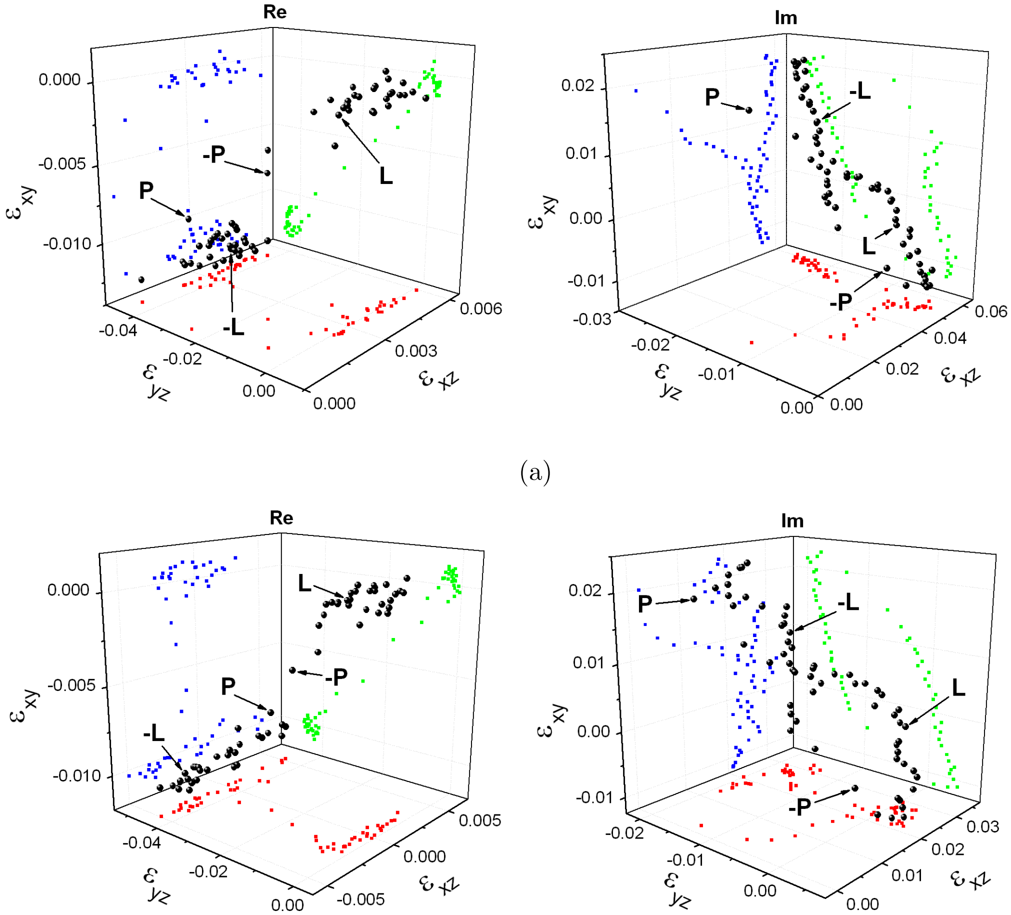

(a)

(b)

Figure 8.8: The magneto-optical tensor elements ε_{xy}, ε_{xz} and ε_{yz} determined by PL loop measurement on the SCTF composites: (a) FeNi SCTFs infiltrated with PMMA ($\phi = 93.9°$); (b)FeNi SCTFs infiltrated with 5 wt% Fe_3O_4 nanoparticles/PMMA ($\phi = 91.6°$). The sphere symbols in black denote the plot of the elements in the 3-dimension coordinate. The square symbols in color denote the plot of the elements in the corresponding 2-dimension coordinates. P, L and T correspond to the measurement with magnetic field in the laboratory coordinate directions x, y and z respectively while -P, -L and -T denote the directions -x, -y and -z. The arrows indicate the elements obtained by P, L, T and -P, -L, -T measurements.

8.4 Summary

The magnetic properties of the FeNi SCTFs infiltrated with PMMA and FeNi SCTFs infiltrated with 5 wt% Fe_3O_4 nanoparticles/PMMA were investigated by AGFM and MOGE. The hysteresis loop measurements in different configurations reveal a strongly anisotropic nature of the magnetization within the samples. The easier magnetization occurred in the samples with the external magnetic field $\mathbf{H} \perp \mathbf{a}$ axis and $\parallel$ substrate surface. The MOKE of the samples was measured in polar configuration and the complex MO tensor element ε_{xy}^{MO} was determined in the spectral range from 400 to 1000 nm. VMOGE was employed to study the MO response of the samples. The three complex magneto-optical tensor elements ε_{xy}^{P}, ε_{xz}^{T} and ε_{yz}^{L} determined by TP, LT, and PL measurements were plotted in a 3-dimension coordinate. The plots of the complex tensor elements generally form elliptical loops and the projection of the loops to ε_{xy}-ε_{yz} plane exhibits an elongated shape with the long axis along the same directions for both samples. The difference in loop shapes between the two samples indicates that Fe_3O_4 nanoparticles may infiltrate into the void areas and change the anisotropic MO response of the FeNi SCTFs.

Chapter 9

Conclusions

FeNi Slanted columnar thin films (SCTFs) were infiltrated with PMMA and 5wt% Fe_3O_4 nanoparticles/PMMA. The structural and optical properties of the FeNi SCTF composites were investigated with electron microscopy and generalized ellipsometry (GE). AB-EMA was used to model the GE data. The GE results show that the samples possess a biaxial structure with the c axis along the pointing direction of the nanocolumns. Both GE and SEM analysis indicate that after infiltration the samples possess a top isotropic layer above the slanted nanocolumns and the nanocolumns were approximately 10° more inclined towards the substrate surface. The low void fraction obtained by modeling reveals that an excellent infiltration was achieved. The GE analysis reflects that all the samples have a strongly anisotropic optical property. Due to the excellent material infiltration into the void of SCTFs, the optical constants along the three major axes have enhanced greatly across the investigated spectral range.

The magnetic property of the FeNi SCTF composites were investigated by AGFM and MOGE. The hysteresis loop measurements in different configurations reveal a strongly anisotropic nature of the magnetization within the samples. The easier magnetization occurred in the samples with the external magnetic field $\mathbf{H} \perp \mathbf{a}$ axis and $\parallel$ substrate surface. The MOKE of the samples was measured in polar configuration and the complex MO tensor element ε_{xy}^{MO} was determined in the spectral range from 400 to 1000 nm. VMOGE was employed to study the MO response of the samples. The three complex magneto-optical tensor elements ε_{xy}^{P}, ε_{xz}^{T} and ε_{yz}^{L} determined by TP, LT, and PL measurements were plotted in a

3-dimension coordinate system. The plots of the complex tensor elements generally form elliptical loops and the projection of the loops to ε_{xy}-ε_{yz} plane exhibits an elongated shape with the long axis along the same directions for both samples. The difference in loop shapes between the two samples indicates that Fe_3O_4 nanoparticles may infiltrate into the void areas and change the anisotropic MO response of the FeNi SCTFs.

In this thesis, GE and MOGE have demonstrated great capability of characterizing the structural, optical and MO properties of SCTF composites. The results obtain by using the two techniques have proven that the infiltration of functional materials into the voids can be an effective approach to modify the optical and MO properties of STFs. Due to the changes in optical and MO properties, this method extends the application of STFs in various fields such as sensors or magnetic data storage device.

References

[1] Feynman, R. P. *Caltech Engineering and Science* **23**, 22 (1959). 1

[2] Maynard, A. D. *Nature* **475**, 31 (2011). 1

[3] Löestam, G., Rauscher, H., Roebben, G., Klüttgen, B. S., Gibson, N., Putaud, J., and Stamm, H. *Considerations on a Definition of Nanomaterial for Regulatory Purposes.* JRC Reference Report, Luxembourg, (2010). 1, 12

[4] Balazs, A. C., Emrick, T., and Russell, T. P. *Science* **314**, 1107 (2006). 1

[5] Urbina, M. C., Zinoveva, S., Miller, T., Sabliov, C. M., Monroe, W. T., and Kumar, C. S. S. R. *J. Phys. Chem. C* **112**, 11102 (2008). 1

[6] Robel, I., Kuno, M., and Kamat, P. V. *J. Am. Chem. Soc.* **129**, 4136 (2007). 1

[7] Wu, Y., Wang, D., Zhao, P., Niu, Z., Peng, Q., and Li, Y. *Inorg. Chem.* **50**, 2046 (2011). 1

[8] Yang, S., Feng, X., Wang, L., Tang, K., Maier, J., and Müllen, K. *Angew. Chem. Int. Ed.* **49**, 4795 (2010). 2

[9] Zeng, S., Tang, K., Li, T., Liang, Z., Wang, D., Wang, Y., Qi, Y., and Zhou, W. *J. Phys. Chem. C* **112**, 4836 (2008). 2

[10] Zhao, Y., Ye, D., Wang, G., and Lu, T. *Proceedings of SPIE* **5219**, 59 (2003). 2

[11] Kesapragada, S. V., P., V., Nalamasu, O., and Gall, D. *Nano Lett.* **6**, 854 (2006). 2

[12] Harris, K. D., Huzinga, A., and Brett, M. J. *Electrochem. Solid-State Lett.* **5**, H27 (2002).

[13] Steele, J. J., Gospodyn, J. P., Sit, J. C., and Brett, M. J. *IEEE Sens. J.* **6**, 24 (2006). 2

[14] Bouclè, J., Ravirajan, P., and Nelson, J. *J. Mater. Chem.* **17**, 3141 (2007). 2, 3

[15] Gerein, N. J., Fleischauer, M. D., and Brett, M. J. *Sol. Energ. Mat. Sol. C.* **94**, 2343 (2010). 2

[16] Toader, O. and John, S. *Science* **292**, 1133 (2001). 2

[17] Hodgkinson, I. and Wu, Q. h. *Adv. Mater.* **13**, 889 (2001).

[18] Hrudey, P. C. P., Szeto, B., and Brett, M. J. *Appl. Phys. Lett.* **88**, 251106 (2006).

[19] Robbie, K., Cui, Y., Elliott, C., and Kaminska, K. *Appl. Opt.* **45**, 8298 (2006). 2

[20] Dick, B., Brett, M. J., Smy, T. J., Freeman, M. R., Malac, M., and Egerton, R. F. *J. Vac. Sci. Technol. A* **18**, 1838 (2000). 2

[21] Hawkeye, M. M. and Brett, M. J. *J. Vac. Sci. Technol. A* **25**, 1317 (2007). 2, 3, 6, 7

[22] Schmidt, D., Hofmann, T., Craig Herzinger, M., Schubert, E., and Schubert, M. *Appl. Phys. Lett.* **96**, 091906 (2010). 2, 3

[23] Tang, F., Liu, D., Ye, D., Zhao, Y., Lu, T., Wang, G., and Vijayaraghavan, A. *J. Appl. Phys.* **93**, 4194 (2003). 57

[24] Tang, F., Liu, D., Ye, D., Zhao, Y., Lu, T., and Wang, G. *J. Mag. Mag. Mat.* **283**, 65 (2004). 57

[25] Umlor, M. T. *Appl. Phys. Lett.* **87**, 082505 (2005). 3

[26] Günes, S., Neugebauer, H., and Sariciftci, N. S. *Chem. Rev.* **107**, 1324 (2007). 3

[27] Schmidt, D., Müller, C., Hofmann, T., Inganäs, O., Arwin, H., Schubert, E., and Schubert, M. *Thin Solid Films* **519**, 2645 (2011). 3

[28] Lakhtakia, A., McCall, M. W., Sherwin, J. A., Wu, Q. H., and Hodgkinson, I. J. *Opt. Commun.* **194**, 33 (2001). 3

[29] Robbie, K., Broer, D. J., and Brett, M. J. *Nature* **399**, 764 (1999). 3

[30] Kennedy, S. R., Sit, J. C., Broer, D. J., and Brett, M. J. *Liq. Cryst.* **28**, 1799 (2001). 3

[31] Schubert, E. *CAREER: Chiral Nanostructure Hybrid Materials for Applications in Terahertz Resonator and Magnetic Storage Devices, ECCS-0846329, National Science Foundation Award.* (2009-2014). 3

[32] Tompkins, H. G. and Irene, E. A. *Handbook of Ellipsometry.* William Andrew Publishing, Norwich, (2005). 5, 23, 31, 32, 33

[33] Schubert, M. *Phys. Rev. B* **53**, 4265 (1996). 28, 29, 30

[34] Dressel, M., Gompf, B., Faltermeier, D., Tripathi, A. K., Pflaum, J., and Schubert, M. *Opt. Express* **16**, 19770 (2008).

[35] Schubert, M., Hofmann, T., and Herzinger, C. M. *J. Opt. Soc. Am. A* **16**, 19770 (2008).

[36] Schubert, M. and Dollase, W. *Opt. Lett.* **27**, 2073 (2002).

[37] Schubert, M. *Ann. Phys.* **15**, 480 (2006). 33

[38] Makinistian, L., Albanesi, E. A., Gonzalez Lemus, N. V., Petukhov, A. G., Schmidt, D., Schubert, E., Schubert, M., Losovyj, Y. B., Galiy, P., and Dowben, P. *Phys. Rev. B* **81**, 075217 (2010). 5

[39] Schmidt, D., Booso, B., Hofmann, T., Schubert, E., Sarangan, A., and Schubert, M. *Appl. Phys. Lett.* **94**, 011914 (2009). 5

[40] Schmidt, D., Schubert, E., and Schubert, M. *Phys. Stat. Sol. (a)* **205**, 748 (2008). 53

[41] Schmidt, D., Booso, B., Hofmann, T., Schubert, E., Sarangan, A., and Schubert, M. *Opt. Lett.* **34**, 992 (2009).

[42] Schmidt, D., Kjerstad, A. C., Hofmann, T., Skomski, R., Schubert, E., and Schubert, M. *J. Appl. Phys.* **105**, 113508 (2009). 53

[43] Beydaghyan, G., Buzea, C., Cui, Y., Elliott, C., and Robbie, K. *Appl. Phys. Lett.* **87**, 153103 (2005). 5

[44] Schmidt, D. *Generalized Ellipsometry on Sculptured Thin Films made by Glancing Angle Deposition*. PhD thesis, University of Nebraska-Lincoln, Department of Electrical Engineering, (2010). 5, 7, 10, 11, 26, 27, 31, 32, 39

[45] Nieuwenhuizen, J. M. and Haanstra, H. B. *Philips Tech. Rev.* **27**, 87 (1966). 7

[46] Tait, R. N., Smy, T., and Brett, M. J. *Thin Solid Films* **226**, 196 (1993).

[47] Meakin, P. *Phys. Rev. A* **38**, 994 (1988).

[48] Lichter, S. and Chen, J. *Phys. Rev. Lett.* **56**, 1396 (1986). 7

[49] Hodgkinson, I., Wu, Q. H., and Hazel, J. *Appl. Opt.* **37**, 2653 (1998). 7

[50] Schubert, E., Fahlteich, J., Rauschenbach, B., Schubert, M., Lorenz, M., Grundmann, M., and Wagner, G. *J. Appl. Phys.* **100**, 016107 (2006). 8

[51] Robbie, K. and Brett, M. J. *J. Vac. Sci. Technol. A* **15**, 1460 (1997). 9

[52] Lu, A., Salabas, E. L., and Schüth, F. *Angew. Chem. Int. Ed.* **46**, 1222 (2007). 12, 14, 15, 44

[53] Gupta, A. K. and Gupta, M. *Biomaterials* **26**, 3995 (2005). 12

[54] Mornet, S., Vasseur, S., Grasset, F., Verveka, P., Goglio, G., Demourgues, A., Portier, J., Pollert, E., and Duguet, E. *Prog. Solid State Chem.* **34**, 237 (2006). 12

[55] Li, Z., Wei, L., Gao, M. Y., and Lei, H. *Adv. Mater.* **17**, 1001 (2005). 12

[56] Gass, J., Poddar, P., Almand, J., Srinath, S., and Srikanth, H. *Adv. Funct. Mater.* **16**, 71 (2006). 12, 15

[57] Hyeon, T. *Chem. Commun.* , 927 (2003). 12

[58] Lopez-Santiago, A., Gangopadhyay, P., Thomas, J., Norwood, R. A., Persoons, A., and Peyghambarian, N. *Appl. Phys. Lett.* **95**, 143302 (2009). 12, 16

[59] Elliott, D. W. and Zhang, W. *Environ. Sci. Technol.* **35**, 4922 (2001). 12

[60] Takafuji, M., Ide, S., Ihara, H., and Xu, Z. *Chem. Mater.* **16**, 1977 (2004). 12

[61] Lu, A., Schmidt, W., Matoussevitch, N., Bönnermann, H., Spliethoff, B., Tesche, B., Bill, E., Kiefer, W., and Schüth, F. *Angew. Chem. Int. Ed.* **43**, 4303 (2004). 12

[62] Tsang, S. C., Caps, V., Paraskevas, I., Chadwick, D., and Thompsett, D. *Angew. Chem. Int. Ed.* **43**, 5645 (2004). 12

[63] Gangopadhyay, R. and De, A. *Chem. Mater.* **12**, 608 (2000). 13, 14

[64] Xu, C., Ohno, K., Ladmiral, V., and Composto, R. J. *Polymer* **49**, 3568 (2008). 13

[65] Yong, V. and Hahn, H. *Nanotechnology* **15**, 1338 (2004). 14

[66] Park, M. J. and Char, K. *Langmuir* **22**, 1375 (2006). 14

[67] Tartaj, P., Morales, M. P., Veintemillas-Verdaguer, S., González-Carreño, T., and Serna, C. J. *J. Phys. D: Appl. Phys.* **36**, 182 (2003). 14

[68] Butterworth, M. D., Bell, S. A., Armes, S. P., and Simpson, A. W. *J. Colloid Interface Sci.* **183**, 91 (1996). 14

[69] Wan, M. and Li, J. *J. Polymer. Sci.* **36**, 2799 (1998).

[70] Barratt, G. *Cell. Mol. Life Sci.* **60**, 21 (2003).

[71] Tartaj, P., Morales, M. P., González-Carreño, T., Veintemillas-Verdaguer, S., and Serna, C. J. *J. Magn. Magn. Mater* **28**, 290 (2005). 14

[72] Harris, L. A., Goff, J. D., Carmichael, A. Y., Riffle, J. S., Harburn, J. J., Pierre, T., and Saunders, G. M. *Chem. Mater.* **15**, 1367 (2003). 14

[73] Thunemann, A. F., Schutt, D., Kaufner, L., Pison, U., and Möhwald, H. *Langmuir* **22**, 2351 (2006). 14

[74] Batlle, X. and Labarta, A. *J. Phys. D* **35**, R15 (2002). 15

[75] Sorensen, C. M. *Magnetismin Nanoscale Materials in Chemistry.* Wiley-Interscience Publication, New York, (2001). 15

[76] Wilson, J. L., Poddar, P. N., Frey, A., Srikanth, H., Mohomed, K., Harmon, J. P., Kotha, S., and Wachsmuth, J. *J. Appl. Phys.* **95**, 1439 (2004). 15

[77] Baker, C., Shah, S. I., and Hasanain, S. K. *J. Magn. Magn. Mater.* **280**, 412 (2004). 15

[78] Ceylan, A., Baker, C. C., Hasanain, S. K., and Shah, S. I. *Phys. Rev. B* **72**, 134411 (2005). 16

[79] Kalska, B., Paggel, J. J., Fumagalli, P., Hilgendorff, M., and Giersig, M. *J. Appl. Phys.* **92**, 7481 (2002). 16

[80] Menéndez, J. L., Bescós, B., Armelles, G., Serna, R., Gonzalo, J., Doole, R., and Petford-Long, A. K. *Phys. Rev. B* **65**, 205413 (2002). 16

[81] Moolekamp, F. E. and Stokes, K. L. *IEEE TRANSACTIONS ON MAGNETICS* **45**, 4888 (2009). 17

[82] Kalska, B., Paggel, J. J., Fumagalli, P., Rybczynski, J., Hilgendorff, M., and Giersig, M. *J. Appl. Phys.* **95**, 1343 (2004). 17

[83] Hayashi, K., Fujikawa, R., Sakamoto, W., Inoue, M., and Yogo, T. *J. Phys. Chem. C* **112**, 14255 (2008). 17

[84] Smith, D. A., Barnakov, Y. A., Scott, B. L., White, S. A., and Stokes, K. L. *J. Appl. Phys.* **97**, 10M504 (2005). 17

[85] Dzarova, A., Royer, F., Timko, M., Jamon, D., Kopcansky, P., Kovac, J., Choueikani, F., Gojzewski, H., and Rousseau, J. J. *J. Magn. Magn. Mater.* **323**, 1453 (2011). 17

[86] Cullity, B. D. and Graham, C. D. *Introduction to Magnetic Materials*. John Wiley and Sons Inc, Hoboken, New Jersey, (2009). 19, 20, 35

[87] Fujiwara, H. *Spectroscopic Ellipsometry Principles and Applications*. John Wiley and Sons Ltd, West Sussex, England, (2007). 21, 22, 23, 30

[88] Azzam, R. M. A. and Bashara, N. M. *Ellipsometry and Polarized Light*. North Holland Publ. Co., Amsterdam, (1984). 24

[89] Schubert, M. *Infrared Ellipsometry on Semiconductor Layer Structures: Phonons, Plasmons, and Polaritons*. Springer, Berlin, (2004). 25, 28

[90] de Graef, M. and McHenry, M. E. *Structure of Materials: An Introduction to Crystallogrpahy, Diffraction, and Symmetry*. Cambridge University Press, Cambridge, (2007). 27

[91] Bruggeman, D. A. G. *Ann. Physik* **24**, 636 (1953). 32

[92] Hodgkinson, I. J. and Wu, Q. H. *Birefringent Thin Films and Polarizing Elements.* World Scientific, Singapore, (1997). 32

[93] Visnovsky, S. *Czech. J. Phys. B* **36**, 625 (1986). 33

[94] Martín, J. and Mijangos, C. *Langmuir* **25**, 1181 (2009). 37